Fourier Neural Network Approximation of Transition Densities in Finance

Rong Du * Duy-Minh Dang†

September 8, 2023

Abstract

This paper introduces FourNet, a novel single-layer feed-forward neural network (FFNN) method designed to approximate transition densities for which closed-form expressions of their Fourier transforms, i.e. characteristic functions, are available. A unique feature of FourNet lies in its use of a Gaussian activation function, enabling exact Fourier and inverse Fourier transformations and drawing analogies with the Gaussian mixture model. We mathematically establish FourNet's capacity to approximate transition densities in the L_2-sense arbitrarily well with finite number of neurons. The parameters of FourNet are learned by minimizing a loss function derived from the known characteristic function and the Fourier transform of the FFNN, complemented by a strategic sampling approach to enhance training. Through a rigorous and comprehensive error analysis, we derive informative bounds for the L_2 estimation error and the potential (pointwise) loss of nonnegativity in the estimated densities. FourNet's accuracy and versatility are demonstrated through a wide range of dynamics common in quantitative finance, including Lévy processes and the Heston stochastic volatility models-including those augmented with the self-exciting Queue-Hawkes jump process.

Keywords: transition density, jump processes, neural networks, Fourier transform, option pricing

MSC codes: 62M45, 91-08, 60E10, 62P05

1 Introduction

The application of machine learning, especially deep learning, in quantitative finance has garnered considerable interest. Recent breakthroughs in computational resources, data availability, and algorithmic enhancements have encouraged the adoption of machine learning techniques in various quantitative finance domains. These include, but are not limited to, portfolio optimization [33, 54], asset pricing [56, 4], model calibration and option pricing [51, 34, 24], solution of high-dimensional partial differential equations [21, 26, 55, 49], valuation adjustments [15, 18, 19], as well as aspects of stochastic control and arbitrage-free analysis [27, 45, 8].

Transition (probability) density functions, which are crucial in quantitative finance due to their primary role in governing the dynamics of stochastic processes, often do not admit a closed-form expression. Consequently, the utilization of numerical methods for estimating these density functions becomes necessary. Classical methods include kernel density estimation, as referenced in [43, 47, 17].

*School of Mathematics and Physics, The University of Queensland, St Lucia, Brisbane 4072, Australia, email: rong.du1@uq.net.au

†School of Mathematics and Physics, The University of Queensland, St Lucia, Brisbane 4072, Australia, email: duyminh.dang@uq.edu.au

Yet, surprisingly, the development of neural network (NN) methods for estimating these transition probability density functions is significantly underdeveloped. While some existing NN strategies tackle the associated high-dimensional Kolmogorov partial differential equations (PDEs) using deep NNs, these are primarily black-box in nature. Such methodologies have seen applications in option pricing ([51, 50]) and general Itô diffusions ([20]). While these methods are generally effective and versatile, they come with a major limitation: their model-dependent nature necessitates a constant reformulation of the Kolmogorov PDEs for different stochastic models. In addition, the inherent complexity associated with deploying NNs to solve PDEs might deter their practical application. Furthermore, a notable gap in the NN literature, particularly regarding transition density function estimation, is the limited analysis of estimation error and potential compromise of non-negativity.

In quantitative finance, many popular stochastic models have unknown transition densities; however, their Fourier transforms, i.e. characteristic functions, are often explicitly available via the Lévy-Khintchine formula [28]. This property has been extensively utilized in option pricing through various numerical methods. Prominent among these are the Carr-Madan approach [5], the Convolution (CONV) technique [35], Fourier Cosine (COS) method proposed by [12], Shannon-wavelet methods [44, 10], with the COS method being particularly noteworthy. Specifically, the COS method achieves high-order convergence for piecewise smooth problems. However, within the broader framework of stochastic optimal control, where problems often exhibit complex and non-smooth characteristics, this high-order convergence is unattainable, as noted in [37, 14]. Moreover, the COS method's dependence on the simplicity of the payoff for the calculation of Fourier series coefficients further highlights its limitations in this domain, particularly in multi-dimensional settings. In the same vein of research, recent works on ϵ-monotone Fourier methods for control problems in finance merit attention [14, 38, 37, 36].

In response to the noted observations, this paper sets out to achieve three primary objectives. Firstly, we present a single-layer feed-forward (FF) NN approach to approximate transition densities with closed-form Fourier transforms, facilitating training in the Fourier domain. This approach simplifies the implementation considerably when compared to deeper NN structures. Second, we conduct a rigorous and comprehensive analysis of the L_2 estimation error between the exact and the estimated transition densities obtained through the proposed approach. This methodology, dubbed the Fourier-trained Neural Network method or "FourNet", showcases the benefits of using the Fourier transform in FFNN models. Lastl0y, we validate FourNet's accuracy and versatility across a spectrum of stochastic financial models.

The main contributions of this paper are as follows.

- We establish two key results for FourNet: (i) transition densities can be approximated arbitrarily well in the L_2-sense using a single-layer FFNN with a Gaussian activation function and a finite number of neurons; and (ii) the L_2-error in this approximation remains invariant under the Fourier transform map. Indeed, as shown subsequently herein, this result holds more generally for any function in $L_2(\mathbb{R})$ and a Borel measurable non-sigmoid activation function in $L_1(\mathbb{R}) \cap L_2(\mathbb{R})$.

  FourNet's methodology underscores the potential and efficacy of shallow NN architectures for complex approximation tasks. The inherent invariance under Fourier transformation opens opportunities for training and error analysis in the Fourier domain, rather than the conventional spatial domain. This unique capability allows us to utilize the the known closed-form expression of the characteristic function and the Fourier transform of the FFNN for an in-depth analysis of the L_2 estimation error.

- Using FourNet, we formulate an approximation for transition densities using a single-layer FFNN equipped with a Gaussian activation function. FourNet's parameters are fine-tuned by minimizing a mean-squared-error (MSE) loss, supplemented with a mean-absolute-error (MAE) regularization. Both the loss function and regularization term stem from the known characteristic function and the Fourier transform of the FFNN. A strategic sampling approach is proposed, maximizing the benefits of MAE regularization.

  We mathematically establish that the L_2 estimation error in FourNet is bounded by various components, namely the theoretical approximation error, the truncation error in the Fourier domain, the error in parameter estimation, and finite sampling error. We also derive informative bounds for the potential (pointwise) loss of nonnegativity in FourNet-estimated transition density. This analysis provides valuable insight into the behavior and reliability of the proposed Fourier-trained FFNN, making a case for its robust application.

- We showcase FourNet's accuracy and versatility for a wide range of underlying dynamics common in quantitative finance with a particular emphasis on its applications in option pricing. Specifically, our analysis includes the class of exponential Lévy processes, such as the CGMY model [6], Merton's jump-diffusion model [42], and Kou's asymmetric double exponential model [31], as well as multi-dimensional processes within this class. We also consider the Heston model [23], as well as Heston dynamics augmented with the Queue-Hawkes jump process, which has been recently introduced in [11, 2].

This paper is the first in a series where we will present the FourNet method and its applications. While the current paper focuses on European and Bermudan options, a subsequent paper will extend the application of FourNet to control problems, including portfolio optimization, thereby broadening the scope and application of this innovative method. Although the focus in this work is on the approximation and estimation of transition densities, FourNet's methodology and its comprehensive error analysis are also relevant to the study of Green's functions for parabolic integro-differential equations [16], due to the inherent connection between them.

The remainder of the paper is organized as follows. Section 2 describes the general structure of single-layer FFNNs with non-sigmoid activation functions and an associated universal approximation theorem. In Section 3, we present FourNet, including the two key aforementioned mathematical results, and the associated MSE loss function. An error analysis of FourNet is presented in Section 4, while its training is discussed in Section 5. FourNet's accuracy and versatility are demonstrated in Section 6 through extensive numerical experiments. Section 7 concludes the paper and outlines possible future work.

2 Background on single-layer FFNNs

2.1 Non-sigmoid activation functions

Feed-forward neural networks can be perceived as function approximators comprising of several inputs, hidden layers composed of neurons/nodes, an activation function, and several outputs. This study primarily concentrates on shallow NNs characterized by a single input, a single output, and a number of nodes within the hidden layer. We also consider only the case that the input is one dimensional. Figure 2.1 depicts a single-layer FFNN having a total of N nodes in the hidden layer.

We now start with FFNNs with (Borel measurable) non-sigmoid activation functions, and the associated Universal Approximation Theorem [40][Theorem 2.1]. This class of of FFNNs is defined

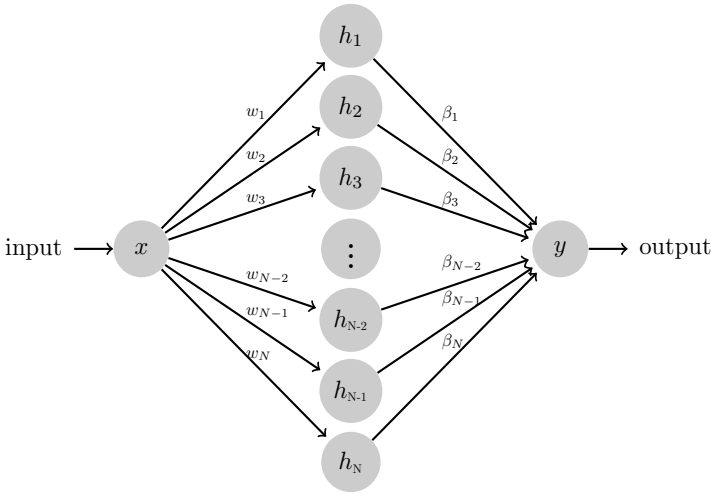

FIGURE 2.1: *Fully connected FFNN (biases not shown) with a single (hidden) layer and a one-dimensional input $x \in R$*

below.

Definition 2.1 ($\Sigma^\dagger(\varphi)$ - activation function φ)**.** *Let $\Sigma^\dagger(\varphi)$ be the class of single-layer FFNNs having arbitrary Borel measurable activation functions φ defined by*

$$\Sigma^\dagger(\varphi) = \left\{ \widehat{g} : \mathbb{R} \to \mathbb{R} \middle| \ \widehat{g}(x;\theta) = \sum_{n=1}^{N} \beta_n \varphi\left(w_n x + b_n\right), \ \beta_n, w_n, b_n \in \mathbb{R} \right\}. \tag{2.1}$$

Here, $x \in \mathbb{R}$ is the input; for a fixed N, the parameter $\theta \in \mathbb{R}^{3N}$ is constituted by the weights w_n and β_n, and the bias terms b_n, $n = 1, \ldots, N$.

For subsequent use, for $1 \leq p < \infty$, we define the sets of p-integrable and p-locally-integrable functions, respectively denoted by $L_p(\mathbb{R})$ and $L_p(\mathbb{R}, loc)$, as follows

$$\begin{aligned} L_p(\mathbb{R}) &= \left\{ f \in \mathcal{M} \ \middle| \ \|f\|_p \equiv \left[\int |f(x)|^p dx \right]^{1/p} < \infty \right\}, \\ L_p(\mathbb{R}, loc) &= \left\{ f \in \mathcal{M} \ \middle| \ f\, \mathbb{I}_{[-A,A]} \in L_p(\mathbb{R}), \forall A \in \{1, 2, 3, \ldots\} \right\}. \end{aligned} \tag{2.2}$$

Here, $\mathcal{M}$ is the space of all Borel measurable functions $f : \mathbb{R} \to \mathbb{R}$.[1] Closeness of two elements f_1 and f_2 of $L_p(\mathbb{R}, loc)$ is measured by a metric $\rho_{p,loc}(f_1, f_2)$ defined as follows [40]

$$\rho_{p,loc}(f_1, f_2) = \sum_{A=0}^{\infty} \left(2^{-A}\right) \min\left(\left\| (f_1 - f_2)\, \mathbb{I}_{[-A,A]} \right\|_p, 1 \right), \quad f_1, f_2 \in L_p(\mathbb{R}, loc). \tag{2.3}$$

Here, $\mathbb{I}_A(\cdot)$ be an indicator function defined as follows: $\mathbb{I}_A(x) = 1$ if $x \in A$ and zero otherwise. For subsequent use, we also introduce the notion of $\rho_{p,loc}$-denseness for $L_p(\mathbb{R}, loc)$ [40].

Definition 2.2 (ρ_p-denseness, $1 \leq p < \infty$)**.** *A subset $\mathcal{S}$ of $L_p(\mathbb{R}, loc)$ is $\rho_{p,loc}$-dense in $L_p(\mathbb{R}, loc)$) if, for any f_1 in $L_p(\mathbb{R}, loc)$) and any $\varepsilon > 0$, there is a f_2 in $\mathcal{S}$ such that $\rho_{p,loc}(f_1, f_2) < \varepsilon$, where $\rho_{p,loc}(f_1, f_2)$ is defined in* (2.3).

[1] It is straightforward to see that $\mathcal{M}$ contains essentially all functions relevant in practical applications.

2.2 Universal Approximation Theorem

The Universal Approximation Theorem proposed in [25] for sigmoid activation functions play a key theoretical foundation. However, sigmoid activation functions are not necessary for universal approximation as highlighted in [40][Theorem 2.1] - therein, an identical universal approximation theorem to the one in [25] was obtained. The key finding of [40] is that, for sufficiently complex single-layer FFNNs with an arbitrary (Borel measurable) activation function at the hidden layer can approximate an arbitrary function $f(\cdot) \in L_p(\mathbb{R}, loc)$, $1 \leq p < \infty$, arbitrary well provided that the activation function, denoted by $\varphi(x)$, belong to $L_1(\mathbb{R}) \cap L_p(\mathbb{R})$ and $\int_{\mathbb{R}} \varphi(x)dx$ does not vanish. Formally, we state the Universal Approximation Theorem for non-sigmoid activation functions below.

Theorem 2.1 (Universal Approximation Theorem [40][Theorem 2.1]**.** *] Let φ be the (Borel measurable) activation function that belongs to $L_1(\mathbb{R}) \cap L_p(\mathbb{R})$ for $1 \leq p < \infty$. If $\int_{\mathbb{R}} \varphi(x)\ dx \neq 0$, then $\Sigma^\dagger(\varphi)$ is $\rho_{p,loc}$-dense in $L_p(\mathbb{R}, loc)$. Here, $\Sigma^\dagger(\varphi)$ and $\rho_{p,loc}$ are respectively defined in Definitions 2.1 and 2.2.*

In other words, with a sufficiently large number of neurons, a single hidden layer FFNN with an arbitrary (Borel measurable) activation function can approximate an arbitrary function $f \in L_p(\mathbb{R}, loc)$ arbitrarily well, provided that the activation function φ belongs to $L_1(\mathbb{R}) \cap L_p(\mathbb{R})$ and $\int_{\mathbb{R}} \varphi(x)dx \neq 0$.

3 A Fourier-trained network (FourNet)

We denote by $T > 0$ a finite horizon, and let t and Δt be fixed such that $0 \leq t < t + \Delta t \leq T$. For sake of exposition, we focus estimating a time and spatially homogeneous transition density, denoted by $g(\cdot)$ and is represented as $g(x, t + \Delta t; y, t) = g(x - y; \Delta t)$. Such transition densities are characteristic of Lévy processes. Our proposed methodology can also be readily adapted for non-homogeneous cases like the Heston [23] or Heston-Queue-Hawkes models [11, 2], but depending on applications, they might require multiple FFNNs tailored to distinct combinations of initial and terminal values.

For notational simplicity, we momentarily suppress the explicit dependence of the transition density on Δt, denoting $g(\cdot) \equiv g(\cdot; \Delta t) : \mathbb{R} \to \mathbb{R}$ as the transition density we seek to approximate using single-layer FFNNs. The importance of Δt will be highlighted in our applications detailed in Section 6.

Since the transition density $g(\cdot)$ is almost everywhere bounded on $\mathbb{R}$, together with the fact that $g \in L_1(\mathbb{R})$, we have $g \in L_2(\mathbb{R})$. Therefore, we consider approximating a transition density $g \in L_1(\mathbb{R}) \cap L_2(\mathbb{R})$.

3.1 A universal approximation result in $L_2(\mathbb{R})$

We now present a new universal approximation result for functions in $L_2(\mathbb{R})$. Specifically, by invoking Hölder's inequality, it is straightforward to establish that $L_2(\mathbb{R}) \subset L_2(\mathbb{R}, \text{loc})$. A natural question thus emerges: if the function we aim to approximate, f, belongs to $L_2(\mathbb{R})$ rather than $L_2(\mathbb{R}, loc)$, can we identify a FFNN in $\Sigma^\dagger(\phi) \cap L_2(\mathbb{R})$ that approximates f arbitrarily well, in the sense of the Universal Approximation Theorem 2.1? In the forthcoming lemma, we affirmatively address this question. Importantly, this can be achieved with only a finite number of neurons in the network.

Lemma 3.1 ($\rho_{2,loc}$-denseness of $\Sigma^\dagger(\varphi) \cap L_2(\mathbb{R})$, continuous φ)**.** *Let φ be a continuous activation function that belongs to $L_1(\mathbb{R}) \cap L_2(\mathbb{R})$. Assume that $f(\cdot)$ is in $L_2(\mathbb{R})$. For any $\epsilon > 0$, there exists a neural network $f'(\cdot; \theta') \in \Sigma^\dagger(\phi) \cap L_2(\mathbb{R})$ with a finite number of neurons such that $\rho_{2,loc}(f, f') < \epsilon$, where $\rho_{2,loc}(\cdot)$ is defined in Definition 2.3.*

Proof of Lemma 3.1. Since φ is in $L_1(\mathbb{R}) \cap L_2(\mathbb{R})$, it satisfies the conditions of Theorem 2.1 for $p = 2$. Therefore, it follows from Theorem 2.1 that there exists a neural network $f_1(\cdot; \theta_h) \in \Sigma^\dagger(\phi)$ such that

$\rho_{2,loc}(f, f_1) < \epsilon$. We also note that since φ is continuous, it follows that all neural networks in $\Sigma^\dagger(\phi)$ are continuous in the parameters.

Next, we show that either the neural network f_1 is in $L_2(\mathbb{R})$ or it can be approximated arbitrarily well by a neural network $f_2 \in \Sigma^\dagger(\phi) \cap L_2(\mathbb{R})$. For this part, to highlight the important role of the number of neurons, we write $f_1(\cdot; \theta(N_1))$, where N_1 is the number of neurons of the neural network f_1.

If $N_1 < \infty$, then, since f_1 is in $L_2(\mathbb{R}, loc)$, and it has to be true that β_n is finite for all $n = 1, \ldots, N_1$. This observation, together with the fact that $\varphi \in L_2(\mathbb{R})$, confirms that f_1 is also in $L_2(\mathbb{R})$.

If $N_1 = \infty$, then $\exists N_2 < \infty$ such that $f_2(\cdot; \theta(N_2)) \in L_2(\mathbb{R})$, and $\rho_{2,loc}(f_1, f_2) < \epsilon$. Setting $f'(\cdot; \theta')$ to either $f_1(\cdot; \theta(N_1))$ or $f_2(\cdot; \theta(N_2))$ completes the proof. □

3.2 Gaussian activation function e^{-x^2}

For the remainder of the paper, unless specified differently, the activation function is defined as $\varphi(x) \equiv \phi(x) = e^{-x^2}$. It is straightforward to verify that $\phi(x) = e^{-x^2}$ is in $L_1(\mathbb{R}) \cap L_2(\mathbb{R})$, and thus satisfies the conditions of Theorem 2.1 for $p = 2$. By Lemma 3.1, for any $\epsilon > 0$, there exists $\widehat{g}(\cdot; \theta^*_\epsilon) \in \Sigma^\dagger(\phi) \cap L_2(\mathbb{R})$ with a finite number of neurons ($N < \infty$) such that $\rho_{2,loc}(g, \widehat{g}) < \epsilon$. Here, in the notation θ^*_ϵ, the subscript ϵ is to emphasize the dependence of the parameter on ϵ.

Since $\widehat{g}(\cdot; \theta^*_\epsilon) \in L_2$ and $N < \infty$, it follows that $|\beta^*_n| < \infty$, $\forall n \leq N$. In addition, it must be true that $w^*_n, b^*_n < \infty$ and $\beta^*_n \neq 0$, $\forall n \leq N$; otherwise the corresponding neuron output is zero, i.e. $\beta^*_n \exp(-(w^*_n x + b^*_n)^2) = 0$. Lastly, it is also the case that $w^*_n \neq 0$ for all $n \leq N$. Otherwise, for some $n \leq N$, $0 < |\beta^*_n| \exp(-(w^*_n x + b^*_n)^2) \leq c$, where $c > 0$ is a finite constant, contradicting with that $\widehat{g}(x; \theta^*_\epsilon) \in L_2$.

Therefore, we conclude that Θ, the space of possible parameters for this FFNN, is constrained by some upper and lower bounds as follows

$$\Theta = \big\{\theta \in \mathbb{R}^{3N} \;\big|\; 0 < |\beta_n| < \beta_{\max},\ 0 < w_{\min} < |w_n| < w_{\max},\ |b_n| < b_{\max},\ \max_{n \leq N}(\beta_n) > 0,\ \text{where}\ \ 0 < \beta_{\max}, w_{\max}, b_{\max} < \infty;\ n = 1, \ldots, N < \infty\big\}. \tag{3.1}$$

We note that, because of the boundedness of the parameter space Θ, for any $\epsilon > 0$, there exists a sufficiently large $A > 0$, such that

$$\sup_{\theta \in \Theta} \int_{\mathbb{R} \setminus [-A, A]} (\widehat{g}(x; \theta))^2 \, dx < \epsilon, \qquad \Theta \text{ defined in (3.1)}. \tag{3.2}$$

We now formally define the set of single-layer FFNNs within which we seek an FFNN approximation of the exact transition density.

$$\Sigma(\phi) = \left\{\widehat{g}(; \theta) \in \Sigma^\dagger(\phi) \text{ defined in (2.1)}, \phi(x) = e^{-x^2} \middle| \theta \in \Theta \text{ defined in (3.1)}\right\}. \tag{3.3}$$

3.3 Existence and invariance of FourNet

We now establish a key result demonstrating the existence of $\widehat{g}(\cdot; \theta^*_\epsilon) \in \Sigma(\phi)$, where $\Sigma(\phi)$ is defined in (3.3), that is capable of approximating the exact transition density $g(\cdot)$ arbitrarily well in the L_2 sense. We hereafter refer to $\widehat{g}(\cdot; \theta^*_\epsilon)$ as a theoretical FFNN approximation to the true transition density $g(\cdot)$. Furthermore, we also show that the associated theoretical approximation error in L_2 remains invariant under the Fourier transform map.

To this end, we recall that the transition density $g(\cdot)$ and the associated characteristic function $G(\eta)$ are a Fourier transform pair. They are defined as follows

$$\mathfrak{F}[g(\cdot)](\eta) \equiv G(\eta) = \int_{-\infty}^{\infty} e^{i\eta x} \, g(x) \, dx, \quad \mathfrak{F}^{-1}[G(\cdot)](x) \equiv g(x) = \frac{1}{2\pi} \int_{-\infty}^{\infty} e^{-i\eta x} \, G(\eta) \, d\eta.$$

For subsequent discussions, for a complex-valued function $f : \mathbb{R} \to \mathbb{C}$, we denote by $\mathrm{Re}_f(\cdot)$ and $\mathrm{Im}_f(\cdot)$ its real and imaginary parts. We also that $|f(\cdot)|^2 = f(\cdot)\overline{f(\cdot)}$, where $\overline{f(\cdot)}$ is the complex conjugate of $f(\cdot)$.

We will also utilize the Plancherel Theorem, which is sometimes also referred to as the Parseval-Plancherel identity [57, 1, 30]. For the sake of convenience, we reproduce it below. Let $f : \mathbb{R} \to \mathbb{R}$ be a function in $L_1(\mathbb{R}) \cap L_2(\mathbb{R})$. The Plancherel Theorem states that its Fourier transform $\mathfrak{F}[f(\cdot)](\eta)$ is in $L_2(\mathbb{R})$, and

$$\int_{\mathbb{R}} |f(x)|^2 \, dx = \frac{1}{2\pi} \int_{\mathbb{R}} |\mathfrak{F}[f(\cdot)](\eta)|^2 \, d\eta. \tag{3.4}$$

Theorem 3.1 (FourNet's existence result)**.** *Given any $\epsilon > 0$, there exists a FFNN $\widehat{g}(\cdot; \theta_\epsilon^*) \in \Sigma(\phi)$, where $\Sigma(\phi)$ is defined in* (3.3)*, that satisfies the following inequality*

$$\int_{\mathbb{R}} |g(x) - \widehat{g}(x; \theta_\epsilon^*)|^2 \; dx = \frac{1}{2\pi} \int_{\mathbb{R}} \left| G(\eta) - \widehat{G}(\eta; \theta_\epsilon^*) \right|^2 \; d\eta \; < \; \epsilon. \tag{3.5}$$

Here, $\widehat{G}(\eta; \theta_\epsilon^*)$ is the Fourier transform of $\widehat{g}(\cdot; \theta_\epsilon^*)$, i.e. $\widehat{G}(\eta; \theta_\epsilon^*) = \mathfrak{F}\left[\widehat{g}(\cdot; \theta_\epsilon^*)\right](\eta)$.

Proof of Theorem 3.1. We first show $\int_{\mathbb{R}} |g(x) - \widehat{g}(x; \theta_\epsilon^*)|^2 \; dx < \epsilon$, then the equality in (3.5).

Since $g(\cdot)$ and $\widehat{g}(\cdot; \theta_\epsilon^*)$ are in $L_2(\mathbb{R})$, there exists A' sufficiently large such that

$$\int_{\mathbb{R}\setminus[-A',A']} |g(x)|^2 \; dx \; < \; \epsilon/8, \quad \int_{\mathbb{R}\setminus[-A',A']} |\widehat{g}(x; \theta_\epsilon^*)|^2 \; dx \; < \; \epsilon/8. \tag{3.6}$$

By Lemma 3.1, there exists $\widehat{g}(x; \theta_\epsilon^*) \in \Sigma\left(\phi\right)$ such that

$$\rho_{2,loc}\left(g, \widehat{g}\left(\cdot; \theta_\epsilon^*\right)\right) = \sum_{A=0}^{\infty} 2^{-A} \min\left(\left\| \left(g - \widehat{g}(\cdot; \theta_\epsilon^*)\right) \mathbb{I}_{[-A,A]} \right\|_2, 1 \right) < \frac{\epsilon^{1/2}}{2^{1/2}} 2^{-A'}.$$

Therefore,

$$2^{-A'} \min\left(\left\| \left(g - \widehat{g}(\cdot; \theta_\epsilon^*)\right) \mathbb{I}_{[-A',A']} \right\|_2, 1 \right) < \frac{\epsilon^{1/2}}{2^{1/2}} 2^{-A'}.$$

from which, we have

$$\int_{[-A',A']} \left(g(x) - \widehat{g}(x; \theta_\epsilon^*)\right)^2 \; dx < \epsilon/2. \tag{3.7}$$

Using (3.6)-(3.7), we have $\int_{\mathbb{R}} \left(g(x) - \widehat{g}(x; \theta_\epsilon^*)\right)^2 \; dx = \ldots$

$$\begin{aligned} \ldots &= \int_{[-A',A']} |g(x) - \widehat{g}(x; \theta_\epsilon^*)|^2 \; dx + \int_{\mathbb{R}\setminus[-A',A']} |g(x) - \widehat{g}(x; \theta_\epsilon^*)|^2 \; dx \\ &< \epsilon/2 + \int_{\mathbb{R}\setminus[-A',A']} 2\left| g(x)^2 + \widehat{g}(x; \theta_\epsilon^*)^2 \right| \; dx < \epsilon, \end{aligned} \tag{3.8}$$

as wanted. Next, the equality in (3.5) follows directly from the Plancherel Theorem (3.4), noting $L_1(\mathbb{R})$ and $L_2(\mathbb{R})$ are closed under addition. This completes the proof. □

Remark 3.1. *Theorem 3.1 presents a significant theoretical result, demonstrating that the FourNet can approximate the exact transition density $g(\cdot)$ within an error of any given magnitude in the L_2-sense. Interestingly, this error is invariant under the Fourier transform, tying together FourNet's approximation capabilities in both spatial and Fourier domains. This invariance opens opportunities for training and error analysis in the Fourier domain instead of the spatial domain. In particular, it enables us to utilize the known closed-form expression of the characteristic function $G(\cdot)$, a process we elaborate on in subsequent sections.*

3.4 Loss function

Recall that $\widehat{g}(x;\theta)$ in $\Sigma(\phi)$ has the form

$$\widehat{g}(x;\theta) = \sum_{n=1}^{N} \beta_n \phi\left(w_n x + b_n\right), \quad \phi(x) = \exp(-x^2), \quad \theta \in \Theta. \tag{3.9}$$

We let $\widehat{G}(\cdot;\theta)$ be the Fourier transform of $\widehat{g}(\cdot;\theta)$, i.e. $\widehat{G}(\eta;\theta) = \mathfrak{F}\left[\widehat{g}(\cdot;\theta)\right](\eta)$. It is straightforward to obtain

$$\widehat{G}(\eta;\theta) = \mathrm{Re}_{\widehat{G}}(\eta;\theta) + i\mathrm{Im}_{\widehat{G}}(\eta;\theta), \text{ where} \tag{3.10}$$

$$\mathrm{Re}_{\widehat{G}} = \sum_{n=1}^{N} \frac{\beta_n\sqrt{\pi}}{w_n} \cos\left(\frac{\eta b_n}{w_n}\right) \exp\left(\frac{-\eta^2}{4w_n^2}\right), \ \mathrm{Im}_{\widehat{G}} = \sum_{n=1}^{N} \frac{\beta_n\sqrt{\pi}}{w_n} \sin\left(\frac{-b_n\eta}{w_n}\right) \exp\left(\frac{-\eta^2}{4w_n^2}\right).$$

Recall that our starting point is that $G(\cdot)$, the Fourier transform of the transition density $g(\cdot)$ is known in closed form. Therefore, motivated by Theorem 3.1, the key step of our methodology is to use the known data $\{(\eta, \mathrm{Re}_G(\eta))\}$ and $\{(\eta, \mathrm{Im}_G(\eta))\}$ to train $\widehat{G}(\eta;\theta)$ using the expressions in (3.10).

To this end, we restrict the domain of η from $\mathbb{R}$ to a fixed finite interval $[-\eta', \eta']$, where $0 < \eta' < \infty$ and is sufficiently large. We denote the total number of training data points by P, and we consider a deterministic, potentially non-uniform, partition $\{\eta_p\}_{p=1}^{P}$ of the interval $[-\eta', \eta']$. With $\delta_p = \eta_{p+1} - \eta_p$, $p = 1, \ldots, P-1$, we assume

$$\delta_{\min} = C_0/P, \quad \delta_{\max} = C_1/P, \quad \text{with } \delta_{\min} = \min_p \delta_p \text{ and } \delta_{\max} = \max_p \delta_p, \tag{3.11}$$

where the constants $C_0, C_1 > 0$ are independent of P. Letting $\widehat{\Theta} \subseteq \Theta$ be the empirical parameter space, we introduce an empirical loss function $\mathrm{Loss}_P(\theta)$, $\theta \in \widehat{\Theta}$, below

$$\mathrm{Loss}_P(\theta) = \frac{1}{P}\sum_{p=0}^{P} \left|G(\eta_p) - \widehat{G}(\eta_p;\theta)\right|^2 + R_P(\theta), \quad \{\eta_p\}_{p=1}^{P} \text{ satisfying (3.11)}. \tag{3.12}$$

Here, $\widehat{G}(\eta_p;\theta)$ is given in (3.10), and $R_P(\theta)$ represents an MAE regularization term expressed as follows

$$R_P(\theta) = \frac{1}{P}\sum_{p=1}^{P} \left(\left|\mathrm{Re}_G(\eta_p;\theta) - \mathrm{Re}_{\widehat{G}}(\eta_p;\theta)\right| + \left|\mathrm{Im}_G(\eta_p;\theta) - \mathrm{Im}_{\widehat{G}}(\eta_p;\theta)\right|\right). \tag{3.13}$$

By training $\mathrm{Loss}_P(\cdot)$, we aim to find the empirical minimizer $\widehat{\theta}^* \in \widehat{\Theta}$, where

$$\widehat{\theta}^* = \arg\min_{\theta\in\widehat{\Theta}} \mathrm{Loss}_P(\theta). \tag{3.14}$$

The incorporation of the MAE regularization term is deliberately motivated by our strategic selection of (deterministic) partition points $\{\eta_p\}_{p=1}^{P}$. Specifically, to take full advantage of the closed-form expression of $G(\cdot)$, we choose $\{\eta_p\}_{p=1}^{P}$ to target critical regions of both the real ($\mathrm{Re}_G(\cdot)$) and imaginary ($\mathrm{Im}_G(\cdot)$) parts of $G(\cdot)$. These regions often manifest key characteristics like areas of convexity change, peaks, and other salient features. While the MAE regularization guides the optimization to closely match $G(\cdot)$ at these strategically chosen sampling points, our primary objective remains the minimization of L_2 errors, a crucial aspect for subsequent L_2-error analysis. Details pertaining to selection of $\{\eta_p\}_{p=1}^{P}$ are discussed in Subsection 5.1 and Appendix A.

We conclude that, for deep NNs, the function $\widehat{g}(\cdot;\theta)$ is expressed as a composition of functions. However, computing its Fourier transform can be very complex, as noted by [3]. Yet, our extensive numerical experiments have demonstrated that a single-layer FFNN possesses remarkable estimation capabilities.

Remark 3.2. *Note that, given the boundedness of the parameter space Θ, both $|Re_{\widehat{G}}(\cdot;\theta)|$ and $|Im_{\widehat{G}}(\cdot;\theta)|$, $\theta\in\Theta$, are in $L_1(\mathbb{R})$. We also recall that both $|Re_G(\cdot)|$ and $|Im_G(\cdot)|\in L_1(\mathbb{R})$. Furthermore, since both $g(\cdot)$ and $\widehat{g}(\cdot;\theta)\in\Sigma(\phi)$, for any $\theta\in\Theta$, are in $L_1(\mathbb{R})\cap L_2(\mathbb{R})$, by the Plancherel Theorem (3.4), both $|G(\cdot)|$ and $|\widehat{G}(\cdot;\theta)|$ are in $L_2(\mathbb{R})$. Therefore, for any given $\epsilon>0$, there exists $\eta'>0$ such that, with $f\in\{Re_G, Im_G, Re_{\widehat{G}}(\cdot;\theta), Im_{\widehat{G}}(\cdot;\theta)\}$ and $h\in\{G(\cdot),\widehat{G}(\cdot;\theta)\}$,*

$$\int_{\mathbb{R}\setminus[-\eta',\eta']}|f(\eta)|\,d\eta<\epsilon,\quad \int_{\mathbb{R}\setminus[-\eta',\eta']}|h(\eta)|^2\,d\eta<\epsilon,\quad \forall\theta\in\Theta. \tag{3.15}$$

That is, the truncation error in the Fourier domain can be made arbitrarily small by choosing $\eta'>0$ sufficiently large. In practice, given a closed-form expression for $G(\cdot)$, η' can be determined numerically, as illustrated in Subsection 6.1.

Remark 3.3. *There are two potential interpretations of the methodology outlined above. The first interpretation sees $\widehat{g}(x;\theta)$ in (3.9) as a FFNN approximation of the exact transition density $g(\cdot)$, and its parameters are learned by minimizing the loss function $Loss_P(\theta)$ (defined in (3.12)). Alternatively, $\widehat{g}(x;\theta)$ in (3.9) can be written as*

$$\widehat{g}(x;\theta)=\sum_{n=1}^{N}\frac{1}{\sqrt{2\pi\sigma_n^2}}\exp\left(-\frac{(x-\mu_n)^2}{2\sigma_n^2}\right),\quad \mu_n=-\frac{b_n}{w_n},\ \sigma_n^2=\frac{1}{2w_n^2}. \tag{3.16}$$

This can be essentially viewed as a Gaussian mixture with N components [41], where the n-th Gaussian component has mean $\mu_n=-\frac{b_n}{w_n}$ and variance $\frac{1}{2w_n^2}$. Unlike traditional Gaussian mixtures, the centers of the component distributions are not predetermined but are also learned through training. Finally, it is worth noting that the set of all normal mixture densities is dense in the set of all density functions under the L_1-metric (see [32]), hence a mixture of Gaussian like in (3.16) can be used to estimate any unknown density function.

4 Error analysis

We start by defining relevant quantities for our error analysis. Let $\epsilon>0$ be given. By Theorem 3.1, there exists $\widehat{g}(x;\theta_\epsilon^*)\in\Sigma(\phi)$ such that $\int_{\mathbb{R}}\left|g(x)-\widehat{g}(x;\theta_\epsilon^*)\right|^2 ds<\epsilon$. We will refer to this L_2-error as the theoretical approximation error, and the parameter θ_ϵ^* as the theoretical optimizer. We denote by $\widehat{\theta}$ the parameter learned from training the loss function $\text{Loss}_P(\theta)$, and refer to $\widehat{g}(\cdot;\widehat{\theta})$ as the corresponding estimated transition density. We aim to derive an upper bound for the L_2 estimation error $\int_{\mathbb{R}}|g(x)-\widehat{g}(x;\widehat{\theta})|^2\,dx$. By the Plancherel Theorem (3.4), we have $\int_{\mathbb{R}}|g(x)-\widehat{g}(x;\widehat{\theta})|^2\,dx=\int_{\mathbb{R}}\left|G(\eta)-\widehat{G}(\eta;\widehat{\theta})\right|^2 d\eta$. This underscores the unique advantages of the proposed approach: an error analysis is more suited to the Fourier domain than the spatial domain since we can directly benefit from the loss function $\text{Loss}_P(\theta)$ designed specifically for the Fourier domain.

In our error analysis, we require $C':=\sup_{\eta,\theta}|\partial|G(\eta)-\widehat{G}(\eta;\theta)|^2/\partial\eta|<\infty$, for all $\eta\in[-\eta',\eta']$ and $\theta\in\Theta$. Given that Θ is bounded and thus $\widehat{G}(\eta;\theta)$ possesses a bounded first derivative, the requirement for $C'<\infty$ is that $G(\eta)$ also has a bounded first derivative. This leads us to the assumption that the random variable associated with the density $g(\cdot)$ is absolutely integrable. That is, $\int_{\mathbb{R}}|x|g(x)dx<\infty$.

Therefore, under this assumption, $C' < \infty$. We also recall C_0 and C_1 from (3.11). We now present an error analysis of the FourNet method in Lemma 4.1 below.

Lemma 4.1. *Assume that $\int_{\mathbb{R}} |x|g(x)dx < \infty$. For a given $\epsilon > 0$, let $\widehat{g}(x;\theta_\epsilon^*) \in \Sigma(\phi)$ be a FFNN satisfying*

$$\int_{\mathbb{R}} |g(x) - \widehat{g}(x;\theta_\epsilon^*)|^2 \ dx < \epsilon, \tag{4.1}$$

as per Theorem 3.1. Also, as per Remark 3.2, for a given $\epsilon_1 > 0$, let the truncated Fourier domain $[-\eta', \eta']$ be such that, with $f \in \{Re_G, Im_G, Re_{\widehat{G}}(\cdot;\theta), Im_{\widehat{G}}(\cdot;\theta)\}$ and $h \in \{G(\cdot), \widehat{G}(\cdot;\theta)\}$,

$$\int_{\mathbb{R}\setminus[-\eta',\eta']} |f(\eta)| \ d\eta < \epsilon_1, \quad \int_{\mathbb{R}\setminus[-\eta',\eta']} |h(\eta)|^2 \ d\eta < \epsilon_1, \ \forall \theta \in \Theta. \tag{4.2}$$

Suppose that the parameters $\widehat{\theta}$ learned by training the empirical loss function $Loss_P(\theta)$, $\theta \in \widehat{\Theta}$, defined in (3.12), is such that

$$\Big| \frac{1}{P} \sum_{p=1}^{P} \big|G(\eta_p) - \widehat{G}(\eta_p;\widehat{\theta})\big|^2 + R_P(\widehat{\theta}) - \frac{1}{P} \sum_{p=1}^{P} \big|G(\eta_p) - \widehat{G}(\eta_p;\theta_\epsilon^*)\big|^2 - R_P(\theta_\epsilon^*)\big| < \epsilon_2, \tag{4.3}$$

and the regularization terms $0 < R_P(\theta_\epsilon^*), R_P(\widehat{\theta}) < \epsilon_3$, where $\epsilon_2, \epsilon_3 > 0$. Then,

$$2\pi \int_{\mathbb{R}} \big|g(x) - \widehat{g}(x;\widehat{\theta})\big|^2 \ dx < \frac{2\pi C_1}{C_0}\epsilon + 4\epsilon_1 + C_1(2\epsilon_2 + \epsilon_3) + C'C_1^2 \frac{C_0 + C_1}{C_0 P}. \tag{4.4}$$

Here, $C' = \sup_{\eta \in [-\eta',\eta'], \theta \in \Theta} |\partial |G(\eta) - \widehat{G}(\eta;\theta)|^2 / \partial \eta| < \infty$, C_0 and C_1 are from (3.11).

Proof of Lemma 4.1. For the rest of the proof, we let C be generic positive bounded constant independent of the number of samples P, which may take different values from line to line. Applying the error bound for the composite left-hand-side quadrature rule on a non-uniform partition gives

$$\Big| \sum_{p=1}^{P} \delta_p \big|G(\eta_p) - \hat{G}(\eta_p;\theta)\big|^2 - \int_{[-\eta',\eta']} \big|G(\eta) - \hat{G}(\eta;\theta)\big|^2 \ d\eta \Big| \le C' P (\delta_{\max})^2 = C/P. \tag{4.5}$$

noting $\delta_{\max} = C_1/P$, where $C = C'C_1^2$. Therefore,

$$\begin{aligned}
\int_{\mathbb{R}} \big|G(\eta) \ - \ \widehat{G}(\eta;\widehat{\theta})\big|^2 \ d\eta &\overset{\text{(i)}}{=} \int_{\mathbb{R}\setminus[-\eta',\eta']} \big|G(\eta) - \widehat{G}(\eta;\widehat{\theta})\big|^2 \ d\eta + \int_{[-\eta',\eta']} \big|G(\eta) - \widehat{G}(\eta;\widehat{\theta})\big|^2 \ d\eta \\
&\overset{\text{(ii)}}{<} 4\epsilon_1 + C/P + \frac{C_1}{P} \sum_{p=1}^{P} \Big|G(\eta_p) - \widehat{G}(\eta_p;\widehat{\theta})\Big|^2 \\
&\overset{\text{(iii)}}{<} 4\epsilon_1 + C/P + C_1\big(2\epsilon_2 + \epsilon_3\big) + \frac{C_1}{C_0} \sum_{p=1}^{P} \delta_{\min} \Big|G(\eta_p) - \widehat{G}(\eta_p;\theta_\epsilon^*)\Big|^2 \big) \\
&\overset{\text{(iv)}}{<} 4\epsilon_1 + C/P + C_1\big(2\epsilon_2 + \epsilon_3\big) + \frac{C_1}{C_0}\big(C/P + \int_{[-\eta',\eta']} \big|G(\eta) - \widehat{G}(\eta;\theta_\epsilon^*)\big|^2 d\eta\big) \\
&\overset{\text{(v)}}{<} 4\epsilon_1 + C\big(1 + \frac{C_1}{C_0}\big)/P + C_1(2\epsilon_2 + \epsilon_3) + \frac{2\pi C_1}{C_0} \int_{\mathbb{R}} |g(x) - \widehat{g}(x;\theta_\epsilon^*)|^2 \ dx \\
&\overset{\text{(vi)}}{<} 4\epsilon_1 + C'C_1^2\big(1 + \frac{C_1}{C_0}\big)/P + C_1(2\epsilon_2 + \epsilon_3) + \frac{2\pi C_1}{C_0}\epsilon.
\end{aligned} \tag{4.6}$$

Here, from (i) to (ii), we respectively bound the first and the second terms in (i) by $4\epsilon_1$ using (4.2) and by $C/P+\sum_{p=1}^{P}\delta_{\max}\left|G(\eta_p)-\widehat{G}(\eta_p;\widehat{\theta})\right|^2$, using (4.5) with $\theta=\widehat{\theta}$, noting for all p, $\delta_p\le\delta_{\max}=C_1/P$; to get to (iii), we use (4.3) to bound the last term in (ii) by $C_1(2\epsilon_2+\epsilon_3)+\frac{C_1}{P}\sum_{p=1}^{P}\left|G(\eta_p)-\widehat{G}(\eta_p;\theta^*_\epsilon)\right|^2$, and then replace $\frac{C_1}{P}=\frac{C_1}{C_0}\delta_{\min}$; from (iii) to (iv), noting $\delta_{\min}\le\delta_p$ for all p, we first bound the summation term in (iii) by $\sum_{p=1}^{P}\delta_p\left|G(\eta_p)-\widehat{G}(\eta_p;\theta^*_\epsilon)\right|^2$, which is then further bounded above by $\int_{[-\eta',\eta']}\left|G(\eta)-\widehat{G}(\eta;\theta^*_\epsilon)\right|^2\,d\eta+C'C_1^2/P$ via (4.5) with $\theta=\theta^*_\epsilon$. To get to (v), we bound the (truncated) integral in (iv) by $\int_{\mathbb{R}}|G(\eta)-\hat{G}(\eta;\theta^*_\epsilon)|^2\,d\eta$, which is the same as $2\pi\int_{\mathbb{R}}|g(x)-\widehat{g}(x;\theta^*_\epsilon)|^2\,dx$ by Lemma 3.1. By (4.1), noting $C=C'C_1^2$, we obtain (vi). Finally, by the Plancherel Theorem (3.4) and (4.6), we obtain

$$2\pi\int_{\mathbb{R}}\left|g(x)-\widehat{g}(x;\widehat{\theta})\right|^2\,dx<\frac{2\pi C_1}{C_0}\epsilon+4\epsilon_1+C_1(2\epsilon_2+\epsilon_3)+C'C_1^2\frac{C_0+C_1}{C_0P}.$$

This completes the proof. □

Lemma 4.1[Eqn. (4.4)] decomposes the upper bound for the L_2 estimation error into several error components.

- Theoretical approximation error: assumed to be bounded by ϵ ((4.1)), contributing $\frac{C_1}{C_0}\epsilon$ to the overall error bound.
- Truncation error (Fourier domain): arises from truncating the sampling domain from $\mathbb{R}$ to $[-\eta',\eta']$. It's bounded by ϵ_1 (see (4.2)), with a net contribution of $4\epsilon_1/(2\pi)$ to the derived bound.
- Parameter estimation error: caused by the differences between the learned parameter $\widehat{\theta}$ and the optimal theoretical parameter θ^*_ϵ. It is quantified by differences in loss functions (bounded by ϵ_2) and regularization terms (bounded by ϵ_3). Its total contribution to the error bound is $C_1(\epsilon_2+2\epsilon_3)/(2\pi)$.
- Sampling error: caused by using a finite set of P data points in training. In our analysis, this error is captured through numerical integration error, and is represented as $C'C_1^2\frac{C_0+C_1}{2\pi C_0P}$ in (4.4).

Remark 4.1 (Nonnegativity of $\widehat{g}(\cdot;\widehat{\theta}).$)**.** *We now investigate the potential loss of nonnegativity in $\widehat{g}(\cdot;\widehat{\theta})$, where $\widehat{\theta}$ learned as per Lemma 4.1. To this end, we use $|\min(\widehat{g}(x;\widehat{\theta}),0)|$, for an arbitrary $x\in\mathbb{R}$, as a measure of this potential (pointwise) loss. Following similar steps (i)-(ii) of* (4.5)*, noting $R_P(\widehat{\theta})<\epsilon_3$, we have*

$$\int_{\mathbb{R}}\left(|Re_G(\eta)-Re_{\widehat{G}}(\eta;\widehat{\theta})|+|Im_G(\eta)-Im_{\widehat{G}}(\eta;\widehat{\theta})|\right)\,d\eta<4\epsilon_1+C_1\epsilon_3+C'C_1^2/P,$$

Hence, $|\min(\widehat{g}(x;\widehat{\theta}),0)|\le|g(x)-\widehat{g}(x;\widehat{\theta})|=\frac{1}{2\pi}\left|\int_{\mathbb{R}}e^{-i\eta x}(G(\eta)-\widehat{G}(\eta;\widehat{\theta}))d\eta\right|=\ldots$

$$\ldots\le\frac{1}{2\pi}\int_{\mathbb{R}}|Re_G(\eta)-Re_{\widehat{G}}(\eta;\widehat{\theta})|+|Im_G(\eta)-Im_{\widehat{G}}(\eta;\widehat{\theta})|\,d\eta<\frac{1}{2\pi}\left(4\epsilon_1+C_1\epsilon_3+\frac{C'C_1^2}{P}\right).$$

As demonstrated above, a bound for $|\min(\widehat{g}(x;\widehat{\theta}),0)|$ can also be decomposed into several error components: truncation error ($4\epsilon_1/(2\pi)$), regularization term ($C_1\epsilon_3/(2\pi)$), and sampling error ($C'C_1^2/(2\pi P)$).

The presented analysis offers an in-depth insight into factors influencing the quality of FourNet's approximation for the transition density $g(\cdot)$. It not only emphasizes the necessity for sufficiently large training domains and ample sample sizes but also stresses the importance of efficient sampling techniques and training algorithms. Crucially, it also draws attention to the significance of the coefficients preceding each error component. These coefficients act as markers for the worst-case amplification of individual error components, either in the overall L_2 estimation error or in potential loss of nonnegativity. Consequently, they serve as signposts, guiding us towards areas where we should focus our efforts for more efficient training and, consequently, reduced error.

Of all component, C' attracts special attention. This value is directly related to the oscillatory behavior of $G(\eta)$, highlighting challenges in approximation. Therefore, curtailing C' is an important step toward improving FourNet approximation's quality. In the subsequent section, we discuss a straightforward a linear transformation on the input domain which can effectively temper the oscillatory nature of $G(\eta)$, thereby resulting in significantly improved approximation's quality.

5 Training

We now discuss FourNet's data sampling and training algorithms.

5.1 Linear transformation

As a precursor for subsequent discussions, we consider a random variable $X = \log(S_T)$, where S_t, $t \in [0, T]$, is the time-t underlying asset price following the well-known Heston model [23]. We denote the characteristic function of X by $G_X(\eta) = \mathbb{E}[e^{i\eta X}]$, which is known in closed-form [23, 13].

In Figures 5.1-(a) and (b), we respectively illustrate plots of the real part $\text{Re}_{G_X}(\eta)$ and the imaginary part $\text{Im}_{G_X}(\eta)$ as functions of η. Evidently, both the real and imaginary parts manifest rapid oscillations, presenting significant challenges during NN training. In general, such oscillations lead to numerous local minima and saddle points, erratic gradient behaviors, and difficulty in initialization and learning rates, among other issues.

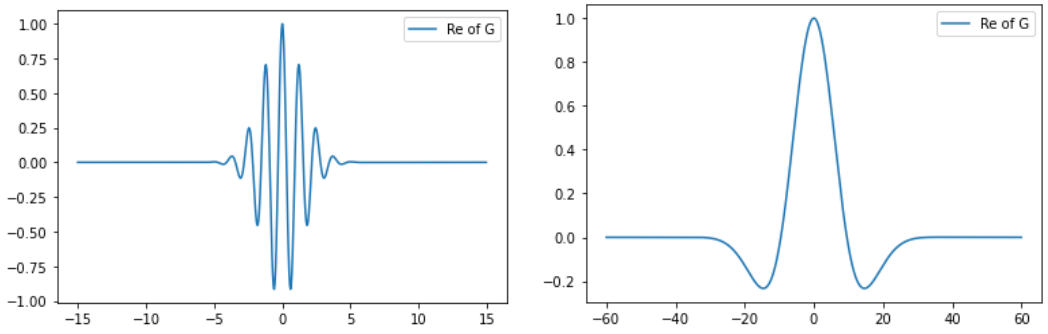

(a) *untransformed* Re_{G_X} (b) *transformed* Re_{G_Y}

FIGURE 5.1: *Comparisons between* $G_X(\eta)$ *and* $G_Y(a\eta)$*, where* $Y = aX + c$*,* $a = 0.15$ *and* $c = -0.6$*. Here,* X *is* $\log(S_T)$*, where* S_t*,* $t \in [0, T]$*, follows the Heston model [23].*

To mitigate rapid oscillations, we propose a linear transformation $Y = aX + c$, yielding $G_Y(\eta) = e^{i\eta c} G_X(a\eta)$. When the random variable is scaled by a, the oscillation frequency in its characteristic function adjusts: oscillations are dampened for $0 < |a| < 1$ and amplified for $|a| > 1$. The component $e^{i\eta c}$ imparts its own oscillatory behavior, which can lead to either partial or significant cancelation of oscillations. Therefore, oscillations in $G_Y(\eta)$ may span larger intervals compared to those in $G_X(\eta)$.

Such broader sampling intervals, however, could necessitate more sample points to accurately capture the behaviors of Re_{G_Y} and Im_{G_Y}, elevating computational cost. The exact manifestation of these effects depends on the synergy between a, c, the oscillations intrinsic to $G_X(\eta)$, and the oscillations introduced by $e^{i\eta c}$. Given these complexities, empirical testing becomes indispensable in determining a suitable combination of a and c. Moreover, with a potentially expanded sampling domain for training, to improve training efficiency, it becomes imperative to judiciously allocate sampling data points in crucial areas of both the Re_{G_Y} and Im_{G_Y}, an approach we will elaborate on in the next subsection.

To illustrate, we adapt the Heston model using $a = 0.15$ and $c = -0.6$ obtained through numerical experiments. The resulting real and imaginary parts of $G_Y(a\eta)$ are presented in Figures 5.1-(c) and (d). Evidently, $G_Y(\eta)$ is more amenable to NN learning compared to $G_X(\eta)$ in Figures 5.1-(a) and (b).

Remark 5.1. *Unless otherwise state, throughout our discussion, the characteristic function $G(\cdot)$ employed for the loss function $\text{Loss}_P(\theta)$ (as defined in (3.12)) corresponds to potentially linearly transformed characteristic function. Specifically, $G(\cdot) = G_Y(\cdot)$, where $Y = aX + c$, where a and c are known real constants. Let $\widehat{g}_Y(y;\widehat{\theta}) = \sum_{n=1}^{N} \widehat{\beta}_n \phi\left(\widehat{w}_n y + \widehat{b}_n\right)$, where $\phi = e^{-x^2}$, be an Fourier-trained FFNN transition density. We can recover the estimated transition density for the random variable X by simply using $\widehat{g}_X(x;\widehat{\theta}) = |a|\widehat{g}_Y(ax + c;\widehat{\theta})$.*

5.2 Sampling data and MAE regularization

Given our prior knowledge of the (potentially linearly transformed) characteristic function $G(\eta)$ in its closed-form, we strategically concentrate spatial sampling points $\{\eta_p\}_{p=1}^{P}$ towards critical regions of $G(\eta)$. These include areas of convexity change, peaks, and other salient characteristics. Such partitioning of the truncated sampling domain $[-\eta', \eta']$ can be achieved via a mapping function, such as the `sinh`$(\cdot)$-based function, which transforms uniform grids into non-uniform ones with more points concentrated in those peaks. It is noteworthy that similar methodologies for point construction have found successful applications as evidenced in [52, 7, 9]. A partitioning scheme that addresses such scenarios with multiple concentration points is presented in Appendix A. We emphasize that a randomly sampled dataset of $\{\eta_p\}_{p=1}^{P}$ might inadequately cover these crucial regions, often requiring a significantly larger dataset for the same precision.

With our strategically defined set $\{\eta_p\}_{p=1}^{P}$ in place, we emphasize the role of the MAE regularization $R_P(\theta)$ in our optimization process. It allows the optimization to focus on concentrating efforts to reduce discrepancies specifically in critical regions while potentially allowing for some discrepancies in less essential areas. Through this, we aim to strike a balance between precision and generalization, thereby curbing potential over-fitting. Our comprehensive numerical tests, presented in Section 6, suggest that this combined approach - strategic sampling based on $G(\cdot)$ characteristics and employing MAE regularization (3.13) - is efficient and robust.

5.3 Training considerations

We briefly describe key considerations in FourNet's training the $\text{Loss}_P(\cdot)$ to obtain the empirical minimizer $\widehat{\theta}^*$. The training of FFNNs is divided into two main stages: the rapid exploration phase and the refinement phase. The initial phase seeks to find a good set of initial weights for the FFNN and fine-tune the baseline learning rate, as these initial weights significantly impact the convergence and accuracy of the training. The refinement phase focuses on further perfecting these weights, often necessitating reduced learning rates to achieve meticulous updates.

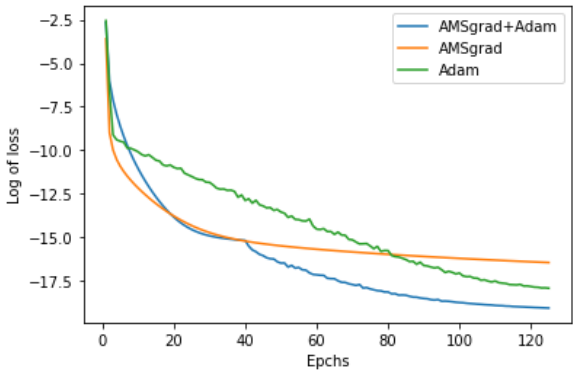

FIGURE 5.2: *Comparisons among AMSgrad+Adam, Adam, and AMSgrad for the loss function* $\text{Loss}_P(\cdot)$ *corresponding to Figures 5.1 (a) and (b).*

Algorithm 5.1 Algorithm for approximating the transition density function $g(\cdot)$ using a FFNN trained in the Fourier domain, given a closed-form expression of the Fourier transform $G(\cdot)$

1: using a closed-form expression of $G(\cdot)$ and numerical integration to find sufficiently large η' as per (3.15);
2: initialize N (number of neurons), P (number of samples); generate $\{\eta_p\}_{p=1}^{P}$ on $[-\eta', \eta']$ using a non-uniform partitioning algorithm (see Algorithm A.1);
3: use AMSgrad optimizer in first training stage to find a good set of initial weights and fine-tune the baseline learning rate;
4: use Adam optimizer in the second training stage
5: construct $\widehat{g}(\cdot, \widehat{\theta})$ with $\widehat{\theta} \in \arg\min_{\theta \in \widehat{\Theta}} \text{Loss}_N(\theta)$, where $\text{Loss}_N(\theta)$ is defined in (3.12);

Due to different focuses of the two stages, choosing the right optimizer for each phase is essential. The Adaptive Moment Estimation (Adam) [29] and AMSGrad with a Modified Stochastic Gradient [53] are standout candidates. Figure 5.2 presents a visual comparative analysis of the performance of these optimizers is compared in terms of reducing the empirical loss function $\text{Loss}_P(\cdot)$ of the NN over a series of training epochs for the case of the Heston model. As illustrated therein, AMSGrad achieves a smoother and steeper reduction in the $\text{Loss}_P(\cdot)$ compared to Adam, especially at higher initial learning rates. However, as the epochs progress, Adam tends to surpass AMSGrad. Our proposed methodology suggests employing AMSGrad during the rapid exploration phase and switching to Adam during the refinement phase.

Putting everything together, a single-layer FFNN algorithm for estimating the transition density by learning its Fourier transform is given in Algorithm (5.1).

6 Numerical experiments

In this section, we demonstrate FourNet's accuracy and versatility through extensive examples. To measure the accuracy of FourNet, we define several (empirical) metrics. Specifically, the closeness of two elements f_1 and f_2 of $L_p(\mathbb{R})$, $p \in \{1, 2\}$, is measured by $L_p(f_1, f_1) = \int_{[-A,A]} |(f_1(x) - f_2(x))|^p \, dx$, for $A > 0$ sufficiently large. In addition, the Maximum Pointwise Error (MPE) is defined by $\text{MPE}(f_1, f_2) = \max_{1 \le k \le K} |f_1(x_k) - f_2(x_h)|$, where $\{x_k\}_{k=1}^{K}$ is the set of evaluation points. Among these, L_2-error

stands out as the principal metric, underscored by the L_2 error analysis presented in Section 4.

In our experiments, unless otherwise stated, all integrals, including those appear in pricing an option, are computed using adaptive Gauss quadrature rule (based on QUADPACK library in Fortran 77 library, `quad` function in Python).

6.1 Setup and preliminary observations

Informed by Remarks 3.2 and 4.1, for all numerical experiments carried out in this paper, the sampling domain $[-\eta', \eta']$ (in the Fourier space), the number of samples P are chosen sufficiently large. Specifically, in computing a sufficiently large η', given a closed-form expression for $G(\cdot)$, we perform numerical integration to estimate η' such that (3.15) corresponding to $G(\cdot)$ is satisfied for a tolerance $\epsilon_1 = 10^{-7}$. That is, with $D = \mathbb{R} \setminus [-\eta', \eta']$,

$$\int_D |\mathrm{Re}_G(\eta)| \, d\eta < \epsilon_1, \quad \int_D |\mathrm{Im}_G(\eta)| \, d\eta < \epsilon_1, \quad \int_D |G(\eta)|^2 \, d\eta < \epsilon_1. \tag{6.1}$$

his typically results in $[-\eta', \eta'] = [-60, 60]$ for all models considered hereafter. The number of samples is taken to be $P = 10^6$. The parameters $\widehat{\theta}$ is learned through training the loss function, and it satisfies $\mathrm{Loss}_P(\widehat{\theta}) \leq 10^{-6}$. This implies that the MAE regularization term $R_P(\theta)$, as defined in (3.13), is less than 10^{-6}.

We observe that the measure for loss of non-negativity $|\min(\widehat{g}(\cdot;\widehat{\theta}), 0)|$ is about 10^{-7}, negligible for all practical purposes. For comparison, we evaluate the bound $\varepsilon = \frac{1}{2\pi}\big(4\epsilon_1 + C_1\epsilon_3 + \frac{C'C_1^2}{P}\big)$, as presented in Remark 4.1. We take $\epsilon_1 = 10^{-7}$ (in accordance with (6.1)), and $\epsilon_3 = 10^{-6}$, given that $\mathrm{Loss}_P(\widehat{\theta}) \leq 10^{-6}$). Considering a uniform partition, we have $\delta_p = 120/P$ for all p. Consequently, $C_1 \geq 120$. Using a conservative estimate, we take $C_1 = 120$, yielding $C_1\epsilon_3 \approx 10^{-4}$ and $\frac{C'C_1^2}{P} \approx C'10^{-2}$. Our numerical findings suggest a notable reduction in the loss of non-negativity when the linear transformation highlighted in Subsection 5.1 is used. This transformation diminishes C', suggesting that $\frac{C'C_1^2}{P} \approx C'10^{-2}$ is the primary contributing term.

We now explore FourNet's accuracy in estimating transition densities a broad array of dynamics commonly encountered in quantitative finance. Subsequently, we will focus on its application for pricing both European and Bermudan options.

6.2 Transition densities

6.2.1 Exponential Lévy processes

We select models that are well-known within the domain of exponential Lévy processes, where the Lévy-Khintchine formula provides a clear representation for the characteristic function $G(\cdot)$ as detailed in [28]. As example, we focus on the Merton jump-diffusion model, introduced by [42], and the CGMY model as proposed by [6]. It's worth noting that the CGMY model can be seen as an extension of the Variance-Gamma model, originally presented in [39]. Additionally, while we conducted tests on the Variance-Gamma model and the Kou jump-diffusion model [31], FourNet consistently proved to be very accurate. In fact, the outcomes from these tests align so closely with those of the highlighted models that we have chosen not to detail them here for the sake of brevity.

In exponential Lévy processes, with $\{S_t\}_{t=0}^T$ being the price process, the process $\{X_t\}_{t=0}^T$, where $X_t = \ln(S_t/S_0)$ is a Lévy process. Relevant to our discussions is the fact that the characteristic function of the random variable X_t is $G_X(\eta) = \exp(t\psi(\eta))$ [28]. As in all numerical examples on transition densities presented in this section, we take $t = T$ which is specified below. The characteristic exponent $\psi(\eta)$ for various exponential Lévy processes considered in this paper are given subsequently.

Merton jump-diffusion dynamics [42] In this case, the characteristic exponent $\psi(\eta)$ is given by $\psi(\eta) = i\left(\mu - \frac{\sigma^2}{2}\right)\eta - \frac{\sigma^2\eta^2}{2} + \lambda\left(e^{i\tilde{\mu}\eta - \tilde{\sigma}^2\eta^2/2} - 1\right)$. In this case, a semi-explicit formula for $g(x;T)$ is given by (see [22][Corollary 3.1])

$$g(x;T) = \sum_{k=0}^{\infty} \frac{e^{-\lambda T}(\lambda T)^k}{k!} g_{\text{norm}}\big(x; \big(\mu - \frac{\sigma^2}{2} - \lambda\kappa\big)T + k\tilde{\mu}, \sigma^2 T + k\tilde{\sigma}^2\big). \tag{6.2}$$

Here, $\kappa = e^{\tilde{\mu}+\tilde{\sigma}^2/2} - 1$, and $g_{\text{norm}}(x;\mu',(\sigma')^2)$ denotes the probability density function of a normal random variable with mean μ' and variance $(\sigma')^2$. The semi-explicit formula given by (6.2) serves as our reference density against which we validate the estimated transition density produced by FourNet. Computationally, we truncate the infinite series in (6.2) to 15 terms. The approximation error resulting from this truncation is approximately 10^{-20}, which is sufficiently small for all practical intents and purposes.

The parameters used for this test case are given in Table (6.1). The linear transform in Remark 5.1 is used with $(a,c) = (0.6, 0.08)$. The number of neurons (N) and L_p/MPE estimation errors by FourNet are presented in Table 6.2, with the principal metric L_2-error highlighted. As evident, FourNet is very accurate with negligible L_2 estimation error (of order 10^{-9}). We note that, without a linear transform, the resulting L_p/MPE estimation errors are much larger. For example, $L_2\left(\text{Re}_G, \text{Re}_{\widehat{G}}\right) = 3.3 \times 10^{-7}$ instead of 1.4×10^{-9} and $L_2\left(\text{Im}_G, \text{Im}_{\widehat{G}}\right) = 1.8 \times 10^{-7}$ vs 1.8×10^{-9}.

Parameters	Values
T (maturity in years)	1
S_0 (initial asset price)	100
r (risk free rate)	0.05
σ (volatility)	0.15
λ (jump intensity)	0.1
$\tilde{\mu}$ (mean of jump size)	-1.08
$\tilde{\sigma}$ (std of jump size)	0.4

TABLE 6.1: *Parameters for the Merton jump diffusion dynamics; values are taken from [14][Table 4].*

N (# of neurons)	45
$L_1\left(\text{Re}_G, \text{Re}_{\widehat{G}}\right)$	2.4×10^{-04}
$L_2\left(\text{Re}_G, \text{Re}_{\widehat{G}}\right)$	1.4×10^{-09}
MPE $\left(\text{Re}_G, \text{Re}_{\widehat{G}}\right)$	1.0×10^{-05}
$L_1\left(\text{Im}_G, \text{Im}_{\widehat{G}}\right)$	5.8×10^{-04}
$L_2\left(\text{Im}_G, \text{Im}_{\widehat{G}}\right)$	1.8×10^{-09}
MPE $\left(\text{Im}_G, \text{Im}_{\widehat{G}}\right)$	2.4×10^{-05}
$L_2\left(g, \widehat{g}\right)$	1.6×10^{-09}

TABLE 6.2: *Estimation errors for the Merton model; parameters from Table 6.1; linear transform in Remark 5.1 used with* $(a,c) = (0.6, 0.08)$.

CGMY model [6] In this case, the characteristic exponent $\psi(\eta)$ is given by $\psi(\eta) = CG(\eta) + i\eta(r + \varpi)$, where $CG(\eta) = C\Gamma(-Y)\left[(M - i\eta)^Y - M^Y + (G + i\eta)^Y - G^Y\right]$ and $\varpi = -CG(-i)$. Here, $\Gamma(\cdot)$ represents the gamma function. In the CGMY model, the parameter should satisfy $C \geq 0$, $G \geq 0$, $M \geq 0$ and $Y < 2$.

The parameters used for this test case are given in Table (6.3). The linear transform in Remark 5.1 is used with $(a,c) = (0.5, 0.0)$. The number of neurons (N) and L_p/MPE estimation errors by FourNet are presented in Table 6.4, with the principal metric L_2-error highlighted. Again, it is clear that FourNet is very accurate. with negligible L_2 estimation error (of order 10^{-8}).

Parameters	Values
T (maturity in years)	1
S_0 (initial asset price)	100
r (risk free rate)	0.1
C (overall activity)	1
G (exp. decay on right)	5
M (exp. decay on left)	5
Y (finite/infinite activity)	0.5

TABLE 6.3: *Parameters for the CGMY dynamics; values taken from [12][Equation 56].*

N (# of neurons)	45
$L_1\left(\mathrm{Re}_G, \mathrm{Re}_{\widehat{G}}\right)$	7.8×10^{-4}
$L_2\left(\mathrm{Re}_G, \mathrm{Re}_{\widehat{G}}\right)$	1.7×10^{-8}
$\mathrm{MPE}\left(\mathrm{Re}_G, \mathrm{Re}_{\widehat{G}}\right)$	3.1×10^{-5}
$L_1\left(\mathrm{Im}_G, \mathrm{Im}_{\widehat{G}}\right)$	2.2×10^{-4}
$L_2\left(\mathrm{Im}_G, \mathrm{Im}_{\widehat{G}}\right)$	1.3×10^{-9}
$\mathrm{MPE}\left(\mathrm{Im}_G, \mathrm{Im}_{\widehat{G}}\right)$	9.2×10^{-6}

TABLE 6.4: *Estimation errors for the CGMY model; parameters from Table 6.3; linear transform in Remark 5.1 is employed with* $(a, c) = (0.5, 0.0)$.

6.2.2 Heston and Heston Queue-Hawkes

Moving beyond exponential L'evy processes, we first evaluate the applicability of FourNet to the Heston model [23], followed by an investigation of the Heston Queue-Hawkes model, as presented in [2]. Notably, for both models, the characteristic functions corresponding to the log-asset price, $\ln(S_t)$, are provided in closed-form expressions.

Parameters	Values
T (maturity in years)	5
S_0 (initial asset price)	100
r (risk free rate)	0.15
σ (volatility of volatility)	0.3
κ (mean-reversion rate)	3
$\bar{V}$ (mean of volatility)	0.09
V_0 (initial volatility)	0.2
ρ (correlation)	0.4

TABLE 6.5: *Parameters for the Heston model; values taken from [10][Table 1].*

N (# of neurons)	45
$L_1\left(\mathrm{Re}_G, \mathrm{Re}_{\widehat{G}}\right)$	1.94×10^{-05}
$L_2\left(\mathrm{Re}_G, \mathrm{Re}_{\widehat{G}}\right)$	6.94×10^{-12}
$\mathrm{MPE}\left(\mathrm{Re}_G, \mathrm{Re}_{\widehat{G}}\right)$	1.18×10^{-06}
$L_1\left(\mathrm{Im}_G, \mathrm{Im}_{\widehat{G}}\right)$	3.91×10^{-05}
$L_2\left(\mathrm{Im}_G, \mathrm{Im}_{\widehat{G}}\right)$	5.22×10^{-11}
$\mathrm{MPE}\left(\mathrm{Im}_G, \mathrm{Im}_{\widehat{G}}\right)$	3.74×10^{-06}

TABLE 6.6: *Estimation errors for the Heston model; parameters from Table 6.5; linear transform in Remark 5.1 is employed with* $(a, c) = (0.15, -0.6)$.

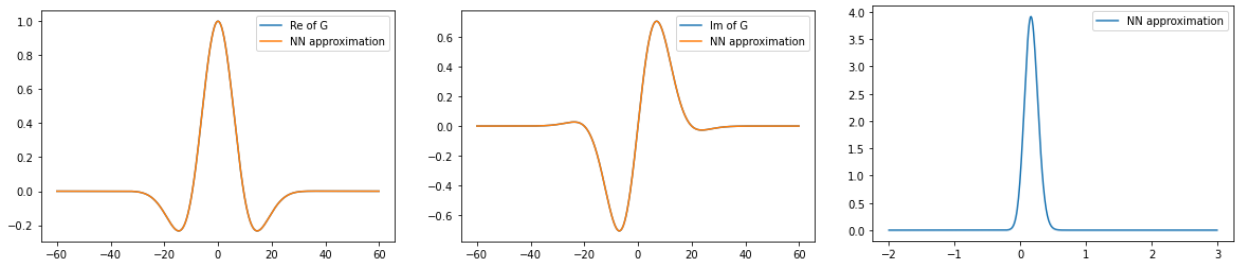

(a) Re_G, $Re_{\widehat{G}}$ (b) Im_G, $Im_{\widehat{G}}$ (c) $\widehat{g}(\cdot; T)$

FIGURE 6.1: *Heston model corresponding to Table 6.5 and Table 6.6.*

Heston model [23] The log-asset price $\ln(S_t)$ and its instantaneous variance V_t follow the dynamics

$$d\ln(S_t) = \big(r - \frac{V_t}{2}\big)dt + \sqrt{V_t}\, dW_t^{(1)}, \quad dV_t = \kappa(\bar{V} - V_t)\, dt + \sigma\sqrt{V_t}\, dW_t^{(2)},$$

with $S_0 > 0$ and $V_0 > 0$ given. Here, $\kappa, \bar{V} > 0$, and $\sigma > 0$ are constants representing the mean-reversion rate, the long-term mean level of the variance, and the instantaneous volatility of the variance; $\{W_t^{(1)}\}$ and $\{W_t^{(2)}\}$ are assumed to be correlated with correlation coefficient $\rho \in [-1, 1]$. As presented in [46][Equation 5], the characteristic function of $X_T = \ln(S_T)$ is given by

$$G_X^{\text{Heston}}(\eta) = \exp^{ir\eta T} \exp\{i\ln(S_0)\eta\} \left(\frac{e^{\kappa T/2}}{\cosh(dT/2) + \xi\sinh(dT/2)/d}\right)^{2\kappa\bar{V}/\sigma^2} \cdot \exp\left\{-V_0 \frac{\big(i\eta + \eta^2\big)\sinh(dT/2)/d}{\cosh(dT/2) + \xi\sinh(dT/2)/d}\right\}, \tag{6.3}$$

where $d = d(\eta) = \sqrt{(\kappa - \sigma\rho i\eta)^2 + \sigma^2\,(i\eta + \eta^2)}$ and $\xi = \xi(\eta) = \kappa - \sigma\rho\eta i$.

Numerical experiments for the Heston model utilize the parameters listed in Table 6.5 (the Feller condition is met). Estimation errors are documented in Table 6.6, noting the linear transformation Remark 5.1. In Figure 6.1, we display plots of the benchmark real part in (a) and the imaginary part in (b). Corresponding estimations by FourNet are also showcased, with the transition density estimated by FourNet depicted in (c). We emphasize FourNet's outstanding performance, particularly evident in the minimal L_2 estimation error.

Heston Queue-Hawkes [11, 2] With $t \in [0, T]$, let $t^{\pm} = \lim_{\epsilon \searrow 0}(t \pm \epsilon)$. Informally, t^- (t^+) denotes the instant of time immediately before (after) calendar time t. The risk-neutral Heston Queue-Hawkes dynamics of the stock price are given by [2]:

$$\begin{aligned} d\left(\frac{S_t}{S_{t^-}}\right) &= (r - \mu_Y\lambda_{t^-})\, dt + \sqrt{V_t}dW_t^{(1)} + (\exp(Y_t) - 1)\, d\pi_t, \\ dV_t &= \kappa(\bar{V} - V_t)dt + \sigma\sqrt{V_t}dW_t^{(2)}. \end{aligned}$$

Here, $\{V_t\}$ is the variance process; $\{W_t^{(1)}\}$, $\{W_t^{(2)}\}$ are correlated standard Brownian motions with the constant correlation $\rho \in [-1, 1]$; $Y_t \sim \text{Normal}(\mu_Y, \sigma_Y^2)$; $\kappa > 0$, $\bar{V} > 0$ and $\sigma > 0$ are the variance's speed of mean reversion, long-term mean, and volatility of volatility parameters, respectively. Finally, $\{\pi_t\}$ is a counting process with stochastic intensity λ_t satisfying the Queue-Hawkes process: $d\lambda_t = \alpha(d\pi_t - d\pi_t^Q)$, where π_t^Q is a counting process with intensity βQ_t, the constants α, and β respectively are the clustering and expiration rates.

The characteristic function of $X_T = \ln(S_T)$ is given by [2][Equation 6]:

$$G_X^{\text{HQH}}(\eta) = G_X^{\text{Heston}}(\eta)\; G_M(\eta). \tag{6.4}$$

Here, $G_X^{\text{Heston}}(\eta)$ is given in (6.3), and $G_M(\eta)$ is defined as follows

$$G_M(\eta) = e^{\frac{\lambda^* T}{2\alpha}(\beta - \alpha - i\alpha\mu_Y\eta - f(\eta))} \cdot \left(\frac{2f(\eta)}{f(\eta) + g(\eta) + e^{-Tf(\eta)}(f(\eta) - g(\eta))}\right)^{\frac{\lambda^*}{\alpha}} \cdot \left(\frac{\big(1 - e^{-Tf(\eta)}\big)\,(2\beta)}{f(\eta) + g(\eta) + e^{-Tf(\eta)}(f(\eta) - g(\eta))}\right)^{Q_0}.$$

Here, $f(\eta) = \sqrt{(\beta + \alpha(1 + i\eta\mu_Y))^2 - 4\alpha\beta\psi_Y(\eta)}$, $g(\eta) = \beta + \alpha(1 + i\eta\mu_Y)$, ψ_Y is the characteristic function of normal random variable with mean μ_Y and std σ_Y.

We conduct numerical experiments using the parameters listed in Table 6.7, with estimation errors detailed in Table 6.8, noting the linear transformation Remark 5.1. Figure 6.1, we present several plots for the benchmark real/imaginary part in (a)/(b) and respective results obtained by FourNet, as well as the estimated transition density in (c). Impressively, FourNet demonstrates outstanding L_2 estimation accuracy.

Parameters	Values
T (maturity in years)	1
S_0 (initial asset price)	9
V_0 (initial volatility)	0.0625
$\bar{V}$ (mean of volatility)	0.16
r (risk free rate)	0.1
σ (volatility of volatility)	0.9
Q_0 (initial value of Q_t)	2
α (clustering rate)	2
β (expiration rate)	3
λ^* (baseline jump intensity)	1.1
μ_Y (mean of jump size)	-0.3
σ_Y (std of jump size)	0.4
ρ (correlation)	0.1

TABLE 6.7: *Parameters for the Heston Queue-Hawkes model. values are taken from [2][Table 1].*

N (# of neurons)	45
$L_1\left(\mathrm{Re}_G, \mathrm{Re}_{\widehat{G}}\right)$	3.36×10^{-4}
$L_2\left(\mathrm{Re}_G, \mathrm{Re}_{\widehat{G}}\right)$	4.19×10^{-9}
$\mathrm{MPE}\left(\mathrm{Re}_G, \mathrm{Re}_{\widehat{G}}\right)$	2.44×10^{-5}
$L_1\left(\mathrm{Im}_G, \mathrm{Im}_{\widehat{G}}\right)$	3.38×10^{-4}
$L_2\left(\mathrm{Im}_G, \mathrm{Im}_{\widehat{G}}\right)$	4.66×10^{-9}
$\mathrm{MPE}\left(\mathrm{Im}_G, \mathrm{Im}_{\widehat{G}}\right)$	1.87×10^{-5}

TABLE 6.8: *Estimation errors for the Heston Queue-Hawkes model; parameters from Table 6.7; linear transform in Remark 5.1 with* $(a, c) = (0.18, -0.31)$ *is applied to* $G_X^{HQH}(\cdot)$ *in* (6.4).

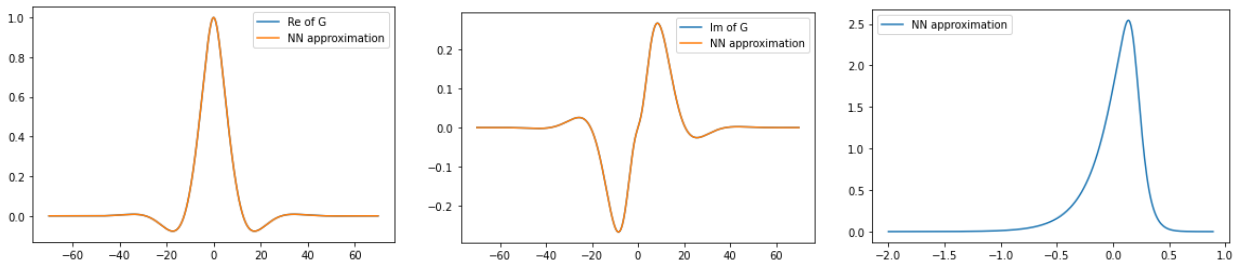

(a) Re_G, $Re_{\widehat{G}}$ (b) Im_G, $Im_{\widehat{G}}$ (c) $\widehat{g}(\cdot; T)$

FIGURE 6.2: *Heston Queue-Hawkes model corresponding to Table 6.7 and Table 6.8.*

6.3 Two-dimensional Merton jump-diffusion process

We now demonstrate the capability of FourNet to two-dimensional Merton jump-diffusion process [48]. The stock prices follow the risk-neutral dynamics

$$dS_t^{(\ell)} = (r - \lambda\kappa^{(\ell)})S_t^{(\ell)}dt + \sigma^{(\ell)}S_t^{(\ell)}dW_t^{(\ell)} + \left(e^{Y^{(\ell)}} - 1\right)S_t^{(\ell)}d\mathcal{P}_t, \ \ell = 1, 2, \tag{6.5}$$

with $S_0^{(\ell)} > 0$ given. Here, $r > 0$ is risk free rate and $\sigma^{(\ell)} > 0$, $\ell = 1, 2$, are instantaneous volatility for the ℓ-underlying; $\{W_t^{(1)}\}$ and $\{W_t^{(2)}\}$ are standard Brown motions with correlation $\rho \in [-1, 1]$; $\{\mathcal{P}_t\}$

is a Poisson process with a constant finite jump arrival rate $\lambda \geq 0$; $[Y^{(1)}, Y^{(2)}]$ are bivariate normally distributed jump sizes with mean $\tilde{\boldsymbol{\mu}} = [\tilde{\mu}^{(1)}, \tilde{\mu}^{(2)}]$ and covariance matrix for the jump components, denoted by $\widetilde{\boldsymbol{\Sigma}}$, where $\widetilde{\boldsymbol{\Sigma}}^{(\ell,k)} = \tilde{\sigma}^{(\ell)}\tilde{\sigma}^{(k)}\tilde{\rho}^{(\ell,k)}$, $\ell, k \in \{1, 2\}$, with $\tilde{\rho}^{(1,2)} = \tilde{\rho}^{(2,1)} = \tilde{\rho} \in [-1, 1]$; $\kappa^{(\ell)} = \mathbb{E}[e^{Y_{(\ell)}} - 1]$, $\ell = 1, 2$.

For subsequent use, we define $\boldsymbol{\mu} = [\mu^{(1)}, \mu^{(2)}]$, where $\mu^{(\ell)} = (r - \lambda\kappa^{(\ell)} - (\sigma^{(\ell)})^2/2)T$, $\ell \in \{1, 2\}$, and covariance matrix for the diffusion components, denoted by $\boldsymbol{\Sigma}$, where $\boldsymbol{\Sigma}^{(\ell,k)} = \sigma^{(\ell)}\sigma^{(k)}\rho^{(\ell,k)}$, $\ell, k \in \{1, 2\}$, with $\rho^{(1,2)} = \rho^{(2,1)} = \rho \in [-1, 1]$.

Parameters	Values
T (maturity in years)	1
σ_1 (volatility)	0.12
σ_2	0.15
r (risk free rate)	0.05
K (strike price)	100
ρ (correlation)	0.3
$\tilde{\rho}$ (jump correlation)	-0.2
λ (jump intensity)	0.6
$\tilde{\mu}_1$ (jump size mean)	-0.1
$\tilde{\mu}_2$	0.1
$\tilde{\sigma}_1$ (jump size std)	0.17
$\tilde{\sigma}_2$	0.13

TABLE 6.9: *Parameters for the 2D Merton jump diffusion. Values are taken from [48] [Parameter sets 2].*

N (# of neurons)	45
$L_2\left(\mathrm{Re}_G, \mathrm{Re}_{\widehat{G}}\right)$	3.15×10^{-8}
$\mathrm{MPE}\left(\mathrm{Re}_G, \mathrm{Re}_{\widehat{G}}\right)$	8.33×10^{-5}
$L_2\left(\mathrm{Im}_G, \mathrm{Im}_{\widehat{G}}\right)$	2.24×10^{-8}
$\mathrm{MPE}\left(\mathrm{Im}_G, \mathrm{Im}_{\widehat{G}}\right)$	4.62×10^{-5}

TABLE 6.10: *Estimation errors for the 2D Merton jump diffusion; parameters from Table 6.9;*

The characteristic function of the random variable $\boldsymbol{X}_T = \left[\ln\left(S_T^{(\ell)}/S_0^{(\ell)}\right)\right]$, $\ell = 1, 2$, is given by [48][Eqn (6.7)]

$$G_{\boldsymbol{X}}(\boldsymbol{\eta}) = \exp\left(i\boldsymbol{\mu}'\boldsymbol{\eta} - \frac{1}{2}\boldsymbol{\eta}'\boldsymbol{\Sigma}\boldsymbol{\eta}\right)\exp\left(\lambda T\left(\exp\left(i\tilde{\boldsymbol{\mu}}'\boldsymbol{\eta} - \frac{1}{2}\boldsymbol{\eta}'\widetilde{\boldsymbol{\Sigma}}\boldsymbol{\eta}\right) - 1\right)\right). \tag{6.6}$$

In this case, it is convenient to write $\widehat{g}(\boldsymbol{x}; \theta)$ in the following form:

$$\widehat{g}(\boldsymbol{x}; \theta) = \sum_{n=1}^{N} \beta_n \frac{1}{(2\pi)|\widehat{\boldsymbol{\Sigma}}_n|^{1/2}} \exp\left(-\frac{1}{2}\left(\boldsymbol{x} - \hat{\boldsymbol{\mu}}_n\right)\hat{\boldsymbol{\Sigma}}_n^{-1}\left(\boldsymbol{x} - \hat{\boldsymbol{\mu}}_n\right)\right).$$

Here, for $n \in N$, $\hat{\boldsymbol{\mu}}_n = [\hat{\mu}_n^{(1)}, \hat{\mu}_n^{(2)}]$, $\widehat{\boldsymbol{\Sigma}}_n$ is the covariance matrix, where $\widehat{\boldsymbol{\Sigma}}_n^{(\ell,k)} = \hat{\sigma}_n^{(\ell)}\hat{\sigma}_n^{(k)}\hat{\rho}_n^{(\ell,k)}$, $\ell, k \in \{1, 2\}$, with $\hat{\rho}_n^{(1,2)} = \hat{\rho}_n^{(2,1)} = \hat{\rho}_n \in [-1, 1]$. The parameters to be learned are: $\{\beta_n, \hat{\mu}_n^{(1)}, \hat{\mu}_n^{(2)}, \hat{\rho}_n\}$, $n = 1, \ldots N$. The real and imaginary parts of the Fourier transform of $\widehat{g}(\boldsymbol{x}; \theta)$ are given by

$$\mathrm{Re}_{\widehat{G}}(\boldsymbol{\eta}) = \sum_{n=1}^{N} \beta_n \cos(\boldsymbol{\eta}'\hat{\boldsymbol{\mu}}_n)\exp\left(\frac{-\boldsymbol{\eta}'\widehat{\boldsymbol{\Sigma}}_n\boldsymbol{\eta}}{2}\right),\ \mathrm{Im}_{\widehat{G}}(\boldsymbol{\eta}) = \sum_{n=1}^{N} \beta_n \sin(\boldsymbol{\eta}'\hat{\boldsymbol{\mu}}_n)\exp\left(\frac{-\boldsymbol{\eta}'\widehat{\boldsymbol{\Sigma}}_n\boldsymbol{\eta}}{2}\right).$$

We conduct numerical experiments using the parameters listed in Table 6.9, with estimation errors detailed in Table 6.10. As evident from Table 6.10, FourNet demonstrates impressive L_2 estimation accuracy.

6.4 Option pricing

We now turn our attention to the application of estimated transition densities produced by FourNet utilized for European and Bermudan option pricing. Recall that $0 \leq t < t + \Delta t \leq T$, where t and Δt are fixed. Typically, in option pricing, we need to approximate a generic convolution integral of the form

$$\begin{aligned} v(x,t) &= e^{-r\Delta t} \int_{\mathbb{R}} v((x'-c)/a, t+\Delta t) g(x-x'; \Delta t)\ dx' \\ &\approx e^{-r\Delta t} \int_{x_{\min}}^{x_{\max}} v((x'-c)/a, t+\Delta t) \widehat{g}(x-x'; \widehat{\theta}, \Delta t)\ dx. \end{aligned} \tag{6.7}$$

Here, $v(\cdot, t+\Delta t)$ is the time-$(t+\Delta t)$ condition; $\widehat{g}(x; \widehat{\theta}, \Delta t)$ is the estimated transition density obtained through FourNet. As we pointed out in Remark 5.1, $\widehat{g}(x; \widehat{\theta}, \Delta t)$ reflects a linear transformation applied to the original density. In light of this, the time-$(t+\Delta t)$ terminal condition must be adjusted correspondingly in the convolution integral, as depicted in (6.7), through $(x'-c)/a$. As noted earlier, this integral is evaluated using adaptive Gauss quadrature rule (based on QUADPACK library in Fortran 77 library, `quad` function in Python). The range $[x_{\min}, x_{\max}]$ for numerical integration will be provided for each test case subsequently.

Strike (E)	Ref. [42]	FourNet `quad`	Rel. error
96	14.83787	14.83790	2×10^{-6}
98	13.43922	13.43925	3×10^{-6}
100	12.10782	12.10785	3×10^{-6}
102	10.84925	10.84928	3×10^{-6}
104	9.66805	9.66808	3×10^{-6}

TABLE 6.11: *European call option prices under the Merton model corresponding to Tables 6.1 and 6.2;* $[x_{\min}, x_{\max}] = [-4, 1]$.

Strike (E)	Ref. [12] (COS)	FourNet `quad`	Rel. error
96	21.78472	21.78466	3×10^{-6}
98	20.77826	20.77819	3×10^{-6}
100	19.81294	19.81288	3×10^{-6}
102	18.88821	18.88815	3×10^{-6}
104	18.00334	18.00328	3×10^{-6}

TABLE 6.12: *European call option prices under CGMY dynamics corresponding to data from Tables 6.3 and 6.4;* $[x_{\min}, x_{\max}] = [-4, 2]$.

Strike (E)	Ref. [23]	FourNet `quad`	Rel. error
96	57.35019	57.35014	1×10^{-6}
98	56.61132	56.61127	1×10^{-6}
100	55.88119	55.88114	1×10^{-6}
102	55.15980	55.15975	1×10^{-6}
104	54.44716	54.44711	1×10^{-6}

TABLE 6.13: *European call option prices under Heston dynamics corresponding to data from Tables 6.5 and 6.6;* $[x_{\min}, x_{\max}] = [-4, 1]$.

Strike (E)	Ref. [12] (COS)	FourNet `quad`	Rel. error
7	4.27369	4.27373	1×10^{-5}
8	3.81734	3.81738	1×10^{-5}
9	3.40704	3.40708	1×10^{-5}
10	3.04018	3.04022	1×10^{-5}
11	2.71399	2.71403	1×10^{-5}

TABLE 6.14: *European call option prices under Heston Queue-Hawkes dynamics; corresponding to data from Tables 6.7 and 6.8;* $[x_{\min}, x_{\max}] = [-3, 1]$

.

6.4.1 European options

For European options, we set $t = 0$ and $\Delta t = T$, and $v(x', t + \Delta t) = v(x', T)$ as the payoff function. The strike of the option is given by $E > 0$. In the context of exponential Lêvy processes examined in this study, which include the Merton and CGMY dynamics, the European call option payoff function is defined as $v\big((x'-c)/a, T\big) \equiv \big(s_0 e^{(x'-c)/a} - E\big)^+$, where E is strike price of the option. For the Heston and Heston Queue-Hawkes models, the European call option payoff is $v\big((s'-c)/a, T\big) = \big(e^{(s'-c)/a} - E\big)^+$.

We provide numerically computed European option prices for the models discussed in the previous section. These are presented in Tables 6.11 (Merton), 6.12 (CGMY), 6.4 (Heston), and 6.4 (Heston Queue-Hawkes). Option prices are derived using the FourNet-estimated transition density $\widehat{g}(s; \widehat{\theta}, \Delta t)$, combined with an adaptive Gauss quadrature rule (the `quad` function in Python) to evaluate the corresponding convolution integral. These results are displayed under the "FourNet-`quad`" column.

Benchmark prices are detailed under the "Ref." column. For the Merton and Heston models, these benchmark prices are determined using the analytical solutions from [42] and the method by [23], respectively. For CGMY, and Heston Queue-Hawkes models, reference European option prices are derived from our implementation of the Fourier Cosine (COS) method [12]. The associated relative errors of these approximations are indicated in the "Rel. error" column. Clearly, the FourNet-`quad` method proves highly accurate, showcasing a negligible error (on the order of 10^{-5}).

6.4.2 Bermudan options

We present a Bermudan put option written on the underlying following the Merton jump-diffusion model [14]. Unlike European options which can only be exercised at maturity, a Bermudan put option can be exercised at any fixed dates t_m^-, $t_m \in \mathcal{T}$, where $\mathcal{T} \equiv \{t_m\}_{m=1}^M$ is a discrete set of pre-determined early exercise dates. We adopt the convention that no early exercise at time t_0. In this example, the early exercise dates are annually apart, that is, $t_{m+1} - t_m = \delta t = 1$ (year), In addition, the underlying asset pays a fixed dividend amount D at t_m^-.

Over each $[t_m, t_{m+1}]$, the pricing algorithm for a Bermudan put option consists of two steps. In Step 1 (time-advancement), we need to approximate the convolution integral (6.7): $v(x, t_m^+) = e^{-r\Delta t} \int_{\mathbb{R}} v((x'-c)/a, t_{m+1}) \widehat{g}(x - x'; \widehat{\theta}, \delta t)\, dx$, for $x \in [x_{\min}, x_{\max}]$, where $x_{\min} < 0 < x_{\max}$, $|x_{\min}|$ and $x_{\max}$ are sufficiently large. In Step 2 (intervention), we impose the condition

$$v(x, t_m) = \max\big(v\big(\ln(\max(e^x - D, e^{x_{\min}})), t_m^+\big), \max(E - e^x, 0)\big). \tag{6.8}$$

Here, E is the strike price, and the expression $\ln(\max(e^x - D, e^{x_{\min}}))$ in (6.8) ensures that the no-arbitrage condition holds, i.e. the dividend paid can not be larger than the stock price at that time, taking into account the localized grid.

In this numerical study, the transition density $g(\cdot; \delta t)$ remains the same across all intervals $[t_m, t_{m+1}]$. Adopting annual early exercise dates, where $\delta t = 1$ year, the transition density $\widehat{g}(\cdot; T = 1)$ as obtained from FourNet (as detailed in Table 6.2 and based on parameters from Table 6.1) is used in Step 1 above. These parameters and those pertaining to the Bermudan put are given in Table 6.15.

Letting $\{x_q\}_{q=0}^Q$ be a partition of $[x_{\min}, x_{\max}]$, we denote by v_q^m a numerical approximation to the exact value $v(x_q, t_m)$, where $t_m \in \mathcal{T} \cup \{t_0\}$. Intermediate value $\{v_q^{m+}\}$, $q = 0, \ldots, Q$, is computed by evaluating the convolution integral in Step 1 via an adaptive Gauss quadrature rule, specifically the `quad` function in Python. The time t_{m+1}-condition $v(\cdot, t_{m+1})$ is given by a linear combination of discrete solutions $\{v_q^{m+1}\}$. For condition (6.8), linear interpolation is then used on $\{v_q^{m+}\}$ to determine the option value $\{v_q^m\}$. Convergence results for the FourNet-quad approach are displayed in Table 6.16,

showcasing evident agreement with an accurate benchmark option price taken from [14][Table 5] (finest grid).

Parameters	Values
S_0 (initial asset price)	100
r (risk free rate)	0.05
σ (volatility)	0.15
λ (jump intensity)	0.1
$\tilde{\mu}$ (mean of jump size)	-1.08
$\tilde{\sigma}$ (std of jump size)	0.4
T (maturity in years)	10
δt (frequency in years)	1
E (strike)	100
D (dividend)	1

TABLE 6.15: *Parameters for the Bermudan put option; values taken from [14][Table 4].*

Q	FourNet-quad	ratio
200	24.8323	
400	24.7903	
800	24.7838	6.7
1600	24.7812	2.5
3200	24.7806	4.3

TABLE 6.16: *Bermudan put option; parameters from Table 6.15; benchmark price: 24.7807, taken from [14][Table 5, finest grid];* $x_{\min} = \ln(S_0) - 10$, $x_{\max} = \ln(S_0) + 10$.

7 Conclusion and future work

This paper has introduced and rigorously analyzed FourNet, a novel single-layer FFNN developed to approximate transition densities with known closed-form Fourier transforms. Leveraging the unique Gaussian activation function, FourNet not only facilitates exact Fourier and inverse Fourier operations, which is crucial for training, but also draws parallels with the Gaussian mixture model, demonstrating its power in approximating sufficiently well a vast array of transition density functions. The hybrid loss function, integrating MSE with MAE regularization, coupled with a strategic sampling approach, has significantly enhanced the training process.

Through a comprehensive mathematical analysis, we demonstrated FourNet's capability to approximate transition densities in the L_2-sense arbitrarily well with a finite number of neurons. We derive informative bounds for the L_2 estimation error and the potential (pointwise) loss of nonnegativity in FourNet-estimated transition densities. We illustrated FourNet's accuracy and versatility through a broad range of models in quantitative finance, including (multi-dimensional) exponential Lévy processes and the Heston stochastic volatility models-including those augmented with the self-exciting Queue-Hawkes jump process. European and Bermudan option prices computed using estimated transition densities obtained through FourNet exhibit impressive accuracy.

Relative to existing methods that leverage the Fourier transform, FourNet distinguishes itself with its straightforward training process and broad applicability. Its effectiveness does not hinge on the simplicity of the value function used to formulate Fourier coefficients, and it adeptly manages multi-dimensional settings. In a subsequent paper, we will extend the application of FourNet to control problems thereby broadening the scope and application of this innovative method. FourNet's simplicity and ease of implementation offer the flexibility to delve into realistic models, previously deemed highly challenging with current frameworks. This includes an investigation of the impact of self-exciting jumps on optimal investment decision in the context of portfolio optimization for Defined Contribution superannuation. This topic is especially relevant in the current climate, marked by rising inflation and economic volatility.

References

[1] Jean-Philippe Anker and Bent Orsted. *Lie Theory: Harmonic Analysis on Symmetric Spaces–General Plancherel Theorems*, volume 230. Springer Science & Business Media, 2006.

[2] Luis A Souto Arias, Pasquale Cirillo, and Cornelis W Oosterlee. A new self-exciting jump-diffusion process for option pricing. *arXiv preprint arXiv:2205.13321*, 2022.

[3] Steven Bergner, Torsten Moller, Daniel Weiskopf, and David J Muraki. A spectral analysis of function composition and its implications for sampling in direct volume visualization. *IEEE transactions on visualization and computer graphics*, 12(5):1353–1360, 2006.

[4] Anastasia Borovykh, Sander Bohte, and Cornelis W Oosterlee. Conditional time series forecasting with convolutional neural networks. *arXiv preprint arXiv:1703.04691*, 2017.

[5] P. Carr and D.B. Madan. Option valuation using the fast Fourier transform. *Journal of Computational Finance*, 2(4):61–73, 1999.

[6] Peter Carr, Hélyette Geman, Dilip B Madan, and Marc Yor. The fine structure of asset returns: An empirical investigation. *The Journal of Business*, 75(2):305–332, 2002.

[7] C. Christara and D.M. Dang. Adaptive and high-order methods for valuing American options. *Journal of Computational Finance*, 14(4):73–113, 2011.

[8] Samuel N Cohen, Christoph Reisinger, and Sheng Wang. Arbitrage-free neural-sde market models. *arXiv preprint arXiv:2105.11053*, 2021.

[9] Duy-Minh Dang, Christina Christara, Kenneth R Jackson, and Asif Lakhany. An efficient numerical PDE approach for pricing foreign exchange interest rate hybrid derivatives. *Journal of Computational Finance*, 18(4).

[10] Duy-Minh Dang and Luis Ortiz-Gracia. A dimension reduction Shannon-wavelet based method for option pricing. *Journal of Scientific Computing*, 75:733–761, 2018.

[11] Andrew Daw and Jamol Pender. An ephemerally self-exciting point process. *Advances in Applied Probability*, 54(2):340–403, 2022.

[12] F. Fang and C.W. Oosterlee. A novel pricing method for European options based on Fourier-Cosine series expansions. *SIAM Journal on Scientific Computing*, 31:826–848, 2008.

[13] Fang Fang and Cornelis W Oosterlee. A Fourier-based valuation method for Bermudan and barrier options under Heston's model. *SIAM Journal on Financial Mathematics*, 2(1):439–463, 2011.

[14] P. A. Forsyth and G. Labahn. An ϵ-monotone Fourier methods for optimal stochastic control in finance. *Journal of Computational Finance*, 22(4):25–71, 2019.

[15] Isabelle Frodé, Viktor Sambergs, and Shengyao Zhu. Neural networks for credit risk and xVA in a front office pricing environment. *Available at SSRN 4136123*, 2022.

[16] M. G. Garroni and J. L. Menaldi. *Green functions for second order parabolic integro-differential problems*. Number 275 in Pitman Research Notes in Mathematics. Longman Scientific and Technical, Harlow, Essex, UK, 1992.

[17] Michael B Giles, Tigran Nagapetyan, and Klaus Ritter. Multilevel Monte Carlo approximation of distribution functions and densities. *SIAM/ASA journal on Uncertainty Quantification*, 3(1):267–295, 2015.

[18] Alessandro Gnoatto, Athena Picarelli, and Christoph Reisinger. Deep xva solver: A neural network–based counterparty credit risk management framework. *SIAM Journal on Financial Mathematics*, 14(1):314–352, 2023.

[19] Ludovic Goudenege, Andrea Molent, and Antonino Zanette. Computing xVA for American basket derivatives by machine learning techniques. *arXiv preprint arXiv:2209.06485*, 2022.

[20] Yiqi Gu, John Harlim, Senwei Liang, and Haizhao Yang. Stationary density estimation of itô diffusions using deep learning. *SIAM Journal on Numerical Analysis*, 61(1):45–82, 2023.

[21] Jiequn Han, Arnulf Jentzen, and Weinan E. Solving high-dimensional partial differential equations using deep learning. *Proceedings of the National Academy of Sciences*, 115(34):8505–8510, 2018.

[22] Zhang Hanwen and Duy-Minh Dang. Monotone numerical integration methods for mean-variance portfolio optimization under jump-diffusion models. *Submitted to Mathematics and Computers in Simulation*, 2023.

[23] S. Heston. A closed form solution for options with stochastic volatility with applications to bond and currency options. *Review of Financial Studies*, 6:327–343, 1993.

[24] PD Hinds and MV Tretyakov. Neural variance reduction for stochastic differential equations. *arXiv preprint arXiv:2209.12885*, 2022.

[25] Kurt Hornik, Maxwell Stinchcombe, and Halbert White. Multilayer feedforward networks are universal approximators. *Neural networks*, 2(5):359–366, 1989.

[26] C. Huré, H. Pham, and X. Warin. Deep backward schemes for high-dimensional nonlinear PDEs. *Mathematics of Computation*, 89(324):1547–1579, 2020.

[27] Kazufumi Ito, Christoph Reisinger, and Yufei Zhang. A neural network-based policy iteration algorithm with global h^2-superlinear convergence for stochastic games on domains. *Foundations of Computational Mathematics*, 21(2):331–374, 2021.

[28] Sato Ken-Iti. *Lévy processes and infinitely divisible distributions*. Cambridge University Press, 1999.

[29] Diederik P Kingma and Jimmy Ba. Adam: A method for stochastic optimization. *arXiv preprint arXiv:1412.6980*, 2014.

[30] T Kobayashi, J Adams, B Lian, and S Sahi. Representation theory and mathematical physics. *Contemporary Mathematics*, 557:23–40, 2011.

[31] Steven G Kou. A jump-diffusion model for option pricing. *Management science*, 48(8):1086–1101, 2002.

[32] Jonathan Li and Andrew Barron. Mixture density estimation. *Advances in neural information processing systems*, 12, 1999.

[33] Yuying Li and Peter A Forsyth. A data-driven neural network approach to optimal asset allocation for target based defined contribution pension plans. *Insurance: Mathematics and Economics*, 86:189–204, 2019.

[34] Shuaiqiang Liu, Anastasia Borovykh, Lech A Grzelak, and Cornelis W Oosterlee. A neural network-based framework for financial model calibration. *Journal of Mathematics in Industry*, 9:1–28, 2019.

[35] R. Lord, F. Fang, F. Bervoets, and C.W. Oosterlee. A fast and accurate FFT-based method for pricing early-exercise options under Lévy processes. *SIAM Journal on Scientific Computing*, 30:1678–1705, 2008.

[36] Y. Lu and D.M. Dang. A pointwise convergent numerical integration method for Guaranteed Lifelong Withdrawal Benefits under stochastic volatility. https://people.smp.uq.edu.au/DuyMinhDang/papers/epsilon_GLWB.pdf, 1 2023. Submitted.

[37] Y. Lu and D.M. Dang. A semi-Lagrangian ϵ-monotone Fourier method for continuous withdrawal GMWBs under jump-diffusion with stochastic interest rate. *Numerical methods for Partial Differential Equations*, 2023. To appear.

[38] Y. Lu, D.M. Dang, P.A. Forsyth, and G. Labahn. An ϵ-monotone Fourier method for Guaranteed Minimum Withdrawal Benefit (GMWB) as a continuous impulse control problem. https://people.smp.uq.edu.au/DuyMinhDang/papers/epsilon_GMWB.pdf, 06 2022. Submitted.

[39] Dilip B Madan and Eugene Seneta. The variance gamma (VG) model for share market returns. *Journal of business*, pages 511–524, 1990.

[40] Stinchcombe Maxwell and White Halbert. Universal approximation using feedforward networks with non-sigmoid hidden layer activation functions. In *International 1989 Joint Conference on Neural Networks*, volume 1, pages 613–617, 1989.

[41] Geoffrey J McLachlan, Sharon X Lee, and Suren I Rathnayake. Finite mixture models. *Annual review of statistics and its application*, 6:355–378, 2019.

[42] Robert C Merton. Option pricing when underlying stock returns are discontinuous. *Journal of financial economics*, 3(1-2):125–144, 1976.

[43] Grigori N Milstein, John GM Schoenmakers, and Vladimir Spokoiny. Transition density estimation for stochastic differential equations via forward-reverse representations. *Bernoulli*, 10(2):281–312, 2004.

[44] Luis Ortiz-Gracia and Cornelis W Oosterlee. A highly efficient Shannon wavelet inverse Fourier technique for pricing European options. *SIAM Journal on Scientific Computing*, 38(1):B118–B143, 2016.

[45] Christoph Reisinger and Yufei Zhang. Rectified deep neural networks overcome the curse of dimensionality for nonsmooth value functions in zero-sum games of nonlinear stiff systems. *Analysis and Applications*, 18(06):951–999, 2020.

[46] Sebastian del Baño Rollin, Albert Ferreiro-Castilla, and Frederic Utzet. A new look at the heston characteristic function. *arXiv preprint arXiv:0902.2154*, 2009.

[47] Murray Rosenblatt. Remarks on some nonparametric estimates of a density function. *The annals of mathematical statistics*, pages 832–837, 1956.

[48] Marjon J Ruijter and Cornelis W Oosterlee. Two-dimensional fourier cosine series expansion method for pricing financial options. *SIAM Journal on Scientific Computing*, 34(5):B642–B671, 2012.

[49] Justin Sirignano and Konstantinos Spiliopoulos. DGM: A deep learning algorithm for solving partial differential equations. *Journal of computational physics*, 375:1339–1364, 2018.

[50] Haozhe Su and David P Newton. Widening the range of underlyings for derivatives pricing with quad by using finite difference to calculate transition densities-demonstrated for the no-arbitrage SABR model. *The Journal of Derivatives*, 28(2):22–46, 2020.

[51] Haozhe Su, Michael V Tretyakov, and David P Newton. Option valuation through deep learning of transition probability density. *arXiv preprint arXiv:2105.10467*, 2021.

[52] Domingo Tavella and Curt Randall. *Pricing financial instruments: The finite difference method*, volume 13. John Wiley & Sons, 2000.

[53] Phuong Thi Tran et al. On the convergence proof of AMSGrad and a new version. *IEEE Access*, 7:61706–61716, 2019.

[54] Pieter M van Staden, Peter A Forsyth, and Yuying Li. A parsimonious neural network approach to solve portfolio optimization problems without using dynamic programming. *arXiv preprint arXiv:2303.08968*, 2023.

[55] E Weinan, Jiequn Han, and Arnulf Jentzen. Algorithms for solving high dimensional PDEs: from nonlinear Monte Carlo to machine learning. *Nonlinearity*, 35(1):278, 2021.

[56] Hongju Yan and Hongbing Ouyang. Financial time series prediction based on deep learning. *Wireless Personal Communications*, 102:683–700, 2018.

[57] K Yosida. Functional analysis, xii+ 465, 1968.

Appendices

A Constructing non-uniform partitions with multiple peaks

In Algorithm A.1, we provide a detailed procedure for constructing non-uniform, yet fixed, partitions of the interval $[\eta_l, \eta_u]$, comprised of M sub-intervals. These partitions feature denser points around a specifically chosen point, $\eta_c \in [\eta_l, \eta_u]$. The parameters d_l and d_u determine the point densities in the intervals $[\eta_l, \eta_c]$ and $[\eta_c, \eta_u]$, respectively, represented as $\frac{1}{d_l}$ and $\frac{1}{d_u}$.

Algorithm A.1 Algorithm for constructing a non-uniform partition of an interval $[\eta_l, \eta_u]$ into M sub-intervals, having a single concentration point, η_c, which is the m-partition point, $m \in \{0, \ldots, M\}$, is fixed.

PartitionOne$(\eta_l, \eta_u, \eta_c, M, m, d_l, d_u)$

1: compute $\alpha_l = \sinh^{-1}\left(\frac{\eta_l - \eta_c}{d_l}\right)$ and $\alpha_u = \sinh^{-1}\left(\frac{\eta_u - \eta_c}{d_u}\right)$;

2: compute $\eta_0 = \eta_l; \eta_j = \eta_c + d_l \sinh(\alpha_l(1 - k_j))$, where $k_j = \dfrac{j}{m}$, $j = 1, \ldots, m$;

3: compute $\eta_j = \eta_c + d_u \sinh(\alpha_u k_j)$, where $k_j = \dfrac{j}{M - m}$, $j = 1, \ldots, (M - m)$;

4: return $Q \equiv \{\eta_j\}_{j=0}^{m} \cup \{\eta_j\}_{j=1}^{M-m}$;

Algorithm A.2 Algorithm for constructing a non-uniform partition of an interval with multiple concentration points.

PartitionMulti$(\eta_{\min}, \eta_{\max}, \{\eta_j\}_{j=1}^{J}, \{P_j\}_{j=1}^{v}, \{q_j\}_{j=1}^{J}, \{\eta_l^j\}_{j=1}^{J}, \{\eta_u^j\}_{j=1}^{J})$

1: $Q_1 \leftarrow PartitionOne\Big(\eta_{\min}, \dfrac{\eta_1 + \eta_2}{2}, \eta_1, P_1, q_1, \eta_l^1, \eta_u^1\Big)$;

2: $Q_j \leftarrow PartitionOne(\dfrac{\eta_{j-1} + \eta_j}{2}, \dfrac{\eta_j + \eta_{j+1}}{2}, \eta_j, P_j, q_j, \eta_l^j, \eta_u^j)$, $j = 2, \ldots, J-1$;

3: $Q_J \leftarrow PartitionOne(\dfrac{\eta_{J-1} + \eta_J}{2}, \eta_{\max}, \eta_J, P_J, q_J, \eta_l^J, \eta_u^J)$;

4: return $Q \equiv \cup_{j=1}^{J} Q_j$;

We use Algorithm A.1 in Algorithm A.2 to generate a non-uniform partition having P sub-intervals for the region $[\eta_{\min}, \eta_{\max}] \equiv [-\eta', \eta']$ with concentration points η_j, $j = 1, \ldots, J$, satisfying $\eta_{\min} \leq \eta_1 < \eta_2 < \ldots < \eta_J \leq \eta_{\max}$. Here, P_j is the number of sub-intervals for the j-th sub-region containing η_j, $j = 1, \ldots, J$, with $\sum_{j=1}^{J} P_j = P$; q_j is the local index of the gridpoint in the j-th sub-region that is equal to η_j; η_l^j and η_u^j are the upper and lower density parameters, respectively, associated with the j-th sub-region containing η_j.